Master Thesis

Possible Plasma Instabilities and Electron Heatings in the Downstream Region of the X-type Neutral Line

Keizo Fujimoto

Department of Geophysics, Graduate School of Science,
Kyoto University

January 2003

Contents

Abstract

A linear analysis and 2-1/2 dimensional full particle simulations are performed to investigate mechanisms of electron heating due to a strong Hall current, which is caused by a large velocity difference between electrons and ions in the outflow region inside the diffusion region associated with the magnetic reconnection process. The numerical solution of the kinetic dispersion relation indicates that the prospective unstable mode varies according to the electron-ion relative velocity V_d; the kinetic cross-field streaming instability (KCSI) is dominant when V_d is under the substantial fraction of the electron thermal velocity v_e, while the electron cyclotron drift instability (ECDI) is first excited for the case where V_d exceeds that critical velocity. The critical drift velocity, where the peak growth rate of the ECDI exceeds that of the KCSI, decreases as the mass ratio increases, since the peak growth rate is almost independent of the mass ratio for the ECDI while it decreases as the mass ratio increases for the KCSI. Our simulation results show that electrons are heated parallel to the ambient magnetic field when the KCSI is excited, because they can be easily trapped along the magnetic field line by the obliquely propagating waves associated with the KCSI. On the other hand, we also show that electrons are heated in the perpendicular direction due to the trapping by the perpendicularly propagating waves assciated with the ECDI. In particular, electrons are quickly heated up to a high temperature when the ECDI is dominant. The electron heating by the ECDI is, however, ineffective when $V_d/v_e < 1$ because the number of resonant electrons, which act to dump the waves, is large in this case.

According to observational data obtained by spacecraft, both instabilities are likely to be excited so that electrons can be heated in either parallel or perpendicular direction depending on the controlling parameters. The identification of the unstable mode will be possible by analyzing the frequencies of excited waves observed by spacecraft.

Chapter 1

Introduction

Plasma heating in space and laboratory experiments is one of the long-standing problems in space physics as well as plasma physics. Magnetic reconnection is, in particular, believed to play an important role in a fast conversion process of the magnetic energy to plasma kinetic energy and be responsible for the plasma heating in the plasma sheet of the Earth. However, the detailed heating mechanism in reconnection is still poorly understood.

In a collisionless reconnection process, the ideal magnetohydrodynamic (MHD) condition breaks down near the X-type neutral line and the diffusion region develops a two-scale structure associated with the electron and ion scales, that is, the electron inertial length λ_e and the ion inertial length λ_i. Outside the diffusion region both electrons and ions are frozen-in to the ambient magnetic field and move together. (In this paper we define the diffusion region as the ion diffusion region otherwise mentioned.) This implies that the studies in the MHD framework can be applied. Indeed, the studies with hybrid simulations [e.g., *Shay et al.*, 1998] and full particle simulations [e.g., *Hesse et al.*, 1999] suggest that the outflow velocity of ions out of the diffusion region never exceed the Alfvén velocity in the inflow region, as expected by *Sweet* [1958] and *Parker* [1963], who predicted it with the use of a resistive MHD description. Furthermore, this fact is also confirmed by the observations with the Geotail spacecraft [*Nagai et al.*, 1998]. On the other hand, inside the diffusion region but outside the electron diffusion region, the difference in motion between electrons and ions becomes important. Since the inertial length of ions λ_i is much larger than that of electrons λ_e, ions are easily unmagnetized even when electrons still remain frozen-in to the magnetic field. This difference allows the electron and ion motion to decouple. In the inflow region, electrons can continue to accelerate with the $\boldsymbol{E} \times \boldsymbol{B}$ drift motion toward the neutral line until they decouple from

the magnetic field in the electron diffusion region. Ions, however, have large gyroradii compared to the scale size of the diffusion region so that they don't execute the $\boldsymbol{E} \times \boldsymbol{B}$ drift motion. This relative motion produces currents, that is, the Hall current system, in the vicinity of the X-type neutral line [*Sonnerup*, 1979]. *Sonnerup* [1979] first predicted the presence of the Hall current system associated with the magnetic reconnection theoretically in which the four current loops resulted in a quadrupole structure in the out-of-plane (dawn-dusk) magnetic field variations. In the past decade, not a few studies with hybrid simulations [e.g., *Mandt et al.*, 1994; *Hesse and Winske*, 1994, 1998; *Lin and Swift*, 1996; *Nakabayashi and Machida*, 1997; *Nakamura et al*, 1998; *Shay et al.*, 1998, 2001] and full particle simulations [e.g., *Tanaka*, 1995; *Hoshino et al.*, 1998, 2001a, b; *Hesse et al.*, 1999] have confirmed the presence of the Hall current system and the associated quadrupole magnetic field structure in the reconnection process. In these studies electrons have been ascertained to play as carriers of the Hall currents. Furthermore, *Nagai et al.* [2001] recently found the Hall current system (the accelerated electrons) and its effect on the magnetic field in the magnetotail of the earth, using magnetic field and plasma measurements onboard the Geotail spacecraft.

In the outflow region just outside the electron diffusion region, where the Hall currents are inward into the neutral line associated with the outward electron flow, electrons are frozen-in to the magnetic field while ions are unmagnetized as mentioned above. This implies that a fluid treatment is still available only to the electrons. Applying the analysis due to *Sweet* [1958] and *Parker* [1963] to the electron diffusion region, we can estimate the upper limit of the outflowing electron velocity as "the electron Alfvén velocity" defined as $V_{Ae} \equiv B_L/\sqrt{\mu_0 m_e n_{ps}}$ [e.g., *Shay et al.*, 2001; *Hoshino et al.*, 2001a], where B_L is the magnetic field in the inflow region, n_{ps} is the plasma density in the plasma sheet (assuming the quasi neutrality, $n_{ps} = n_{i,ps} \simeq n_{e,ps}$, where suffix i and e denote ions and electrons respectively), m_e is the mass of an electron, and μ_0 is the magnetic permeability in vacuum. Thus inside the diffusion region electrons can flow with very high velocity beyond the ordinary Alfvén velocity with which both electrons and ions are expected to flow outside the diffusion region. In fact, *Shay et al.* [2001] confirmed by conducting hybrid simulation that electrons could be accelerated up to approximately the electron Alfvén velocity just outside the electron diffusion region independent of the electron mass. Since the electron motion is basically described by the $\boldsymbol{E} \times \boldsymbol{B}$ drift, it is expected to exist a large relative velocity between electrons and ions across the magnetic field. In such a situation, *Hoshino et al.* [2001b] suggested that the Buneman-like instability might

be excited and electrons would be heated by the unstable waves. However they have not conducted detailed quantitative analyses and it is necessary to identify what kind of instability mode will be actually excited, investigating the kinetic plasma dispersion relation, so as to know the mechanism of the electron heating.

In this paper, we consider locally the outflow region just outside the electron diffusion region and study the possible instabilities excited by a cross-field relative motion with super Alfvénic velocity between electrons and ions, solving the kinetic plasma dispersion relation. We next study the anomalous heating of electrons, using 2-1/2 dimensional electromagnetic full particle simulation with high spatial and time resolution. We show that the expected instability and the resultant mechanism of the electron heating vary according to the value of the cross-field relative velocity between electrons and ions.

Chapter 2

Possible Instabilities : Linear Theory

In order to identify the instabilities excited by a cross-field relative motion between electrons and ions just outside the electron diffusion region, we conduct a linear analysis. We assume the frequency of the unstable waves which are expected to be higher than the ion cyclotron frequency so that ions are unmagnetized. The lower-frequency modes than the ion cyclotron frequency will not have enough time to grow to the appreciable levels inside the diffusion region. Thus the candidates of the unstable modes excited by a cross-field relative drift between electrons and ions are the kinetic cross-field streaming instability (KCSI) [e.g., *Lemons and Gary*, 1977; *Wu et al.*, 1983; *Winske et al.*, 1985], the lower hybrid drift instability (LHDI) [e.g., *Krall and Liewer*, 1971; *Davidson et al.*, 1977; *Huba et al.*, 1978], the electron cyclotron drift instability (ECDI) [e.g., *Wong*, 1970; *Gary and Sanderson*, 1970; *Forslund et al.*, 1970], and the ion acoustic instability [e.g., *Gary*, 1970; *Coroniti et al*, 1977]. However, because we consider the local region so that the effects of gradients in the magnetic field magnitude and density are negligible, the LHDI essentially doesn't arise from our linear analysis. The ion acoustic instability is unlikely to occur in the plasma sheet, where the ion temperature is higher than the electron temperature [e.g., Baumjohann et al., 1989] so that the ion acoustic waves are dumped. Thus, in the following study, we concentrate our attention on the two modes, the KCSI and the ECDI.

2.1 Local Dispersion Relation

To derive a general dispersion relation, in which not only electromagnetic effects are included but also the arbitrary direction of wave propagation and the electron-cyclotron resonance are considered, we follow the procedure by *Tsai et al.* [1983]. We assume wave

frequencies as $\omega_{uh} \gtrsim |\omega| \gtrsim \omega_{lh} >> \omega_{ci}$ in which ions are unmagnetized while electrons are still magnetized, where $\omega_{uh} = (\omega_{pe}^2 + \omega_{ce}^2)^{1/2}$ is the upper hybrid frequency (ω_{pe} and ω_{ce} are the plasma frequency and the cyclotron frequency of electrons respectively.), $\omega_{lh} = (\omega_{ce}\omega_{ci})^{1/2}$ is the lower hybrid frequency, ω_{ci} is the ion cyclotron frequency, and $\omega = \omega_r + i\gamma$ is a complex frequency. We also assume that the electron motion is basically described by the $\boldsymbol{E} \times \boldsymbol{B}$ drift as $\boldsymbol{V}_d = -E_0/B_0\,\hat{\boldsymbol{e}}_x$ while ions are not drifting, where E_0 and B_0 are the ambient 0th-order electric and magnetic fields directed to the y and the $-z$ directions respectively, and $\hat{\boldsymbol{e}}_x$ is the unit vector directed to the x direction. Strictly speaking, ions are expected to conduct the meandering motion and drift to the y direction in the vicinity of the plasma sheet. However the velocity is at most about $0.2\,V_A$ according to the results of a hybrid simulation [*Shay et al.*, 1998], where V_A is the Alfvén velocity in the inflow region, and therefore much lower than the electron drift velocity which is expected to be the substantial fraction of the electron Alfvén velocity V_{Ae} [*Hesse et al.*, 1999; *Shay et al.*, 2001]. Thus we neglect the ion drift motion in the following analysis. We set the wave number vector $\boldsymbol{k}$ in the $x-z$ plane ($\boldsymbol{k} = k_\perp \hat{\boldsymbol{e}}_x + k_\parallel \hat{\boldsymbol{e}}_z$) so as to consider the oblique propagation to the magnetic field. In addition, we assume $k_\perp^2 > k_\parallel^2 >> (\partial \ln B_0/\partial x)^2$, $(\partial \ln n/\partial x)^2$, which justifies the use of the homogeneity approximation in B_0 and n, where n is the local plasma density assuming $n = n_i \simeq n_e$.

We calculate the local dispersion relation in the electron frame so that the uniform electric field E_0 is canceled out and ions possess a bulk velocity $V_d\,\hat{\boldsymbol{e}}_x$. Thus the unperturbed distribution functions of electrons and ions are described as

$$f_{e0} = n\left(\frac{1}{\pi v_e^2}\right)^{\frac{3}{2}} \exp\left[-\frac{v_x^2 + v_y^2 + v_z^2}{v_e^2}\right], \tag{2.1}$$

$$f_{i0} = n\left(\frac{1}{\pi v_i^2}\right)^{\frac{3}{2}} \exp\left[-\frac{(v_x - V_d)^2 + v_y^2 + v_z^2}{v_i^2}\right], \tag{2.2}$$

respectively, where $v_j = (2T_j/m_j)^{1/2}$ is the thermal velocity, T_j and m_j are the temperature and the mass of a particle of species j (=e, i), respectively. Then there exists the following relation between the dielectric tensor $\boldsymbol{\varepsilon}(\boldsymbol{k}, \omega)$ and the fluctuating electric field $\delta\hat{\boldsymbol{E}}$ (see Appendix A for detailed procedure of the derivation), where $\delta\boldsymbol{E} = \delta\hat{\boldsymbol{E}} \exp[i(k_\perp x + k_\parallel z - \omega t)]$,

$$\boldsymbol{D}(\boldsymbol{k}, \omega) \cdot \delta\hat{\boldsymbol{E}} = 0, \tag{2.3}$$

$$\boldsymbol{D}(\boldsymbol{k}, \omega) \equiv \boldsymbol{\varepsilon}(\boldsymbol{k}, \omega) - \left(\frac{ck}{\omega}\right)^2 \left(\boldsymbol{I} - \frac{\boldsymbol{k}\boldsymbol{k}}{k^2}\right),$$

where c is the velocity of light, and $\boldsymbol{I}$ is the unit tensor. We can derive the elements of the dielectric tensor $\boldsymbol{\varepsilon}(\boldsymbol{k},\omega)$ by combining the linearized Vlasov equation and the Maxwell equations (see Appendix A). The dispersion relation which gives the complex eigenfrequency is defined by $\det[\boldsymbol{D}] = 0$, and can be manipulated into the following form,

$$D_{11} + \frac{\frac{2k_\perp^2}{k^2} D_{12}D_{13}D_{23} + D_{12}^2 D_{22} - \frac{k_\perp^2}{k^2} D_{23}^2 D_{22}}{D_{22}D_{33} + \frac{k_\perp^2}{k^2} D_{23}^2} = 0. \tag{2.4}$$

The elements D_{ij} are defined as

$$\begin{aligned}
D_{11} &= 1 + \frac{2\omega_{pi}^2}{k^2 v_i^2}[1 + \xi_i Z(\xi_i)] + \frac{2\omega_{pe}^2}{k^2 v_e^2}\left[1 + \xi_0 e^{-\mu} \sum_{n=-\infty}^{\infty} I_n Z(\xi_n)\right], \\
D_{22} &= 1 - \frac{c^2 k^2}{\omega^2} + \frac{2\omega_{pe}^2}{\omega^2}\mu e^{-\mu} \sum_{n=-\infty}^{\infty} \left\{\frac{n^2}{2\mu^2} I_n + (I_n - I_n')\right\} \xi_0 Z(\xi_n), \\
D_{33} &= 1 - \frac{c^2 k^2}{\omega^2} + \frac{2\omega_{pe}^2}{k^2 v_e^2}\frac{k_\perp^2}{k_\parallel^2}\left[1 + \xi_0 e^{-\mu} \sum_{n=-\infty}^{\infty} \left(1 - n\frac{\omega_{ce}}{\omega}\frac{k^2}{k_\perp^2}\right)^2 I_n Z(\xi_n)\right], \\
D_{12} &= -D_{21} = i\frac{\omega_{pe}^2}{k v_e \omega_{ce}}\frac{k_\perp}{k_\parallel} e^{-\mu} \sum_{n=-\infty}^{\infty} (I_n - I_n') Z(\xi_n), \\
D_{13} &= \frac{k^2}{k_\perp^2} D_{31} = -\frac{2\omega_{pe}^2}{k^2 v_e^2}\frac{k^2}{k_\parallel}\left[1 + \xi_0 e^{-\mu} \sum_{n=-\infty}^{\infty} \left(1 - n\frac{\omega_{ce}}{\omega}\frac{k^2}{k_\perp^2}\right) I_n Z(\xi_n)\right], \\
D_{23} &= -\frac{k^2}{k_\perp^2} D_{32} = i\frac{\omega_{pe}^2}{k v_e \omega_{ce}}\frac{k_\perp}{k_\parallel} e^{-\mu} \sum_{n=-\infty}^{\infty} \left(1 - n\frac{\omega_{ce}}{\omega}\frac{k^2}{k_\perp^2}\right) (I_n - I_n') Z(\xi_n),
\end{aligned} \tag{2.5}$$

where $\xi_n = (\omega - n\omega_{ce})/k_\parallel v_e$, $\xi_i = (\omega - k_\perp V_d)/k v_i$, $\mu = k_\perp^2 v_e^2/2\omega_{ce}^2$, $I_n = I_n(\mu)$ is the modified Bessel function of the nth order, $I_n' = dI_n/d\mu$, $\theta = \tan^{-1}(k_\perp/k_\parallel)$, $k = \sqrt{k_\perp^2 + k_\parallel^2}$, and $Z(\xi) = (\sqrt{\pi})^{-1} \int_{-\infty}^{\infty} dx \exp[-x^2]/(x - \xi)$ is the plasma dispersion function [*Fried and Conte*, 1961]. In Equation (2.4), the first term represents the electrostatic effects while the electromagnetic contributions are lumped into the second term.

2.2 Drift Velocity Dependence

Though many satellite observations in the plasma sheet associated with the magnetic reconnection have been reported in the last decade [e.g., *Baumjohann et al.*, 1991; *Sergeev et al.*, 1995; *Shinohara et al.*, 1998; *Nagai et al.*, 1998, 2001], there is still ambiguity about the values of plasma parameters in the vicinity of the diffusion region and it is difficult

to precisely predict the electron Alfvén velocity in the inflow region (the upper limit of the drift velocity in the outflow region just outside the electron diffusion region) or the electron thermal velocity in the diffusion region. Thus it is necessary to examine how the most unstable mode varies according to the relative drift velocity between electrons and ions. We first solve the dispersion relation (2.4) numerically for the various values of the drift velocity. For calculations we select the values of plasma parameters, $\omega_{ce}/\omega_{pe} = 0.5$, $T_i/T_e = 8.0$, $m_i/m_e = 1836$, and $\beta_i = 1.0$. Figure 1 shows the numerical solutions of the dispersion relation for the various values of the drift velocity. In Figure 1a, the growth rates γ maximized over wavenumber for a fixed value of the propagation angle θ are plotted as a function of θ, for the ECDI (solid curves) and the KCSI (dashed curves), and Figure 1b represents the real frequencies of unstable waves corresponding to Figure 1a. As can be seen in Figure 1a, the peak growth rates of both modes become larger as the drift velocity increases but the enhancement of the growth rates is more rapid for the ECDI than the KCSI. Thus, though the peak growth rate of the KCSI is larger than that of the ECDI at $V_d/v_e = 0.4$, the relation of the magnitudes reverses around $V_d/v_e = 0.6$. Figure 1b indicates that the frequency range of the ECDI and the KCSI is very much different; the KCSI is excited in a frequency a few times larger than the lower hybrid frequency ($\omega_{lh}/\omega_{pe} = 0.012$ in the current parameters), while the ECDI is in a frequency a little above the electron cyclotron frequency ($\omega_{ce}/\omega_{pe} = 0.5$). These results imply that the high frequency mode, the ECDI, dominates the low frequency mode, the KCSI, in the regime where the electron-ion relative velocity exceeds the substantial fraction of the electron thermal velocity.

We also examined the drift velocity dependence in the case of $m_i/m_e = 100$ for application to the numerical simulations shown in the next chapter. In Figure 2, the solutions of Equation (2.4) is shown for the case of $\omega_{ce}/\omega_{pe} = 0.5$, $T_i/T_e = 8.0$, $m_i/m_e = 100$, and $\beta_i = 1.0$. Similar to the case of Figure 1, the peak growth rate of the ECDI becomes larger rapidly as the drift velocity increases, while that of the KCSI shows rather flat variation with a little enhancement. In this case the critical drift velocity, where the peak growth rate of the ECDI exceeds that of the KCSI, is about $1.0\,v_e$, which is larger than $0.6\,v_e$ in the case of $m_i/m_e = 1836$.

2.3 Mass Ratio Dependence of the Critical Velocity

In the previous section, we found that the value of the critical drift velocity was dependent on the mass ratio between an ion and electron, m_i/m_e. Since in the pre-

vious section we considered only the cases of $m_i/m_e = 1836$ (the real mass ratio) and $m_i/m_e = 100$ (for the purpose of application to the simulational study conducted in the next chapter), in this section we derive the general relation between the critical drift velocity and the mass ratio. We assume unstable waves associated with the ECDI to be electrostatic [e.g., *Wong*, 1970; *Gary and Sanderson*, 1970]. Thus the dielectric tensor $\boldsymbol{\varepsilon}(\boldsymbol{k}, \omega)$ can be degenerated into a scalar as

$$\varepsilon_L(\boldsymbol{k}, \omega) = D_{11} = 1 + \frac{2\omega_{pi}^2}{k^2 v_i^2}[1 + \xi_i Z(\xi_i)] + \frac{2\omega_{pe}^2}{k^2 v_e^2}\left[1 + \xi_0 e^{-\mu} \sum_{n=-\infty}^{\infty} I_n Z(\xi_n)\right]. \tag{2.6}$$

The unstable waves in association with the ECDI have a little higher frequencies than the upper harmonics of the electron cyclotron frequency (viz. $\omega_r > n\omega_{ce}$) and propagate almost perpendicularly to the ambient magnetic field (viz. $k_\parallel \simeq 0$). These characteristics of the unstable waves and the condition $(\omega_{ce}/\omega_{pe})^2 << 1$ allow us to set $\xi_n >> 1$ and $\mu >> 1$. Making use of the relation $e^{-\mu} I_n(\mu) \simeq 1/\sqrt{2\pi\mu}$ for the large μ approximation, we can derive the growth rate of the ECDI as

$$\gamma_{ECDI} \simeq \frac{1}{2} \frac{\mathrm{Im} Z'(\xi_i)}{\frac{1}{kv_i}\left[\mathrm{Re} Z(\xi_i) + \xi_i \mathrm{Re} Z'(\xi_i)\right] + \frac{1}{\sqrt{\pi} k v_e} \frac{T_i}{T_e} \frac{n\omega_{ce}^2}{(\omega_r - n\omega_{ce})^2}}, \tag{2.7}$$

where $Z'(\xi_i) = dZ(\xi_i)/d\xi_i = -2[1 + \xi_i Z(\xi_i)]$. The most unstable wave with the ECDI has frequency around $\omega_r \simeq k(V_d - 0.7 v_i)$ [*Forslund et al.*, 1972], which leads to $\xi_i \simeq -0.7$. Since it is the fundamental mode ($n = 1$) that has the peak growth rate according to the results obtained in the previous section, we assume $kV_d \simeq \omega_{ce}$. Then Equation (2.7) can be manipulated into more convenient form, and the peak growth rate of the ECDI over $\omega - k$ plane is expressed as the following form,

$$\frac{\gamma_{ECDI}^M}{\omega_{ce}} \simeq \frac{3}{4\sqrt{\pi}} \left(\frac{V_d}{v_e}\right) \left(\frac{T_e}{T_i}\right) \left[1 + \frac{3}{2\sqrt{\pi}} \left(\frac{V_d}{v_e}\right)^2 \left(\frac{T_e}{T_i}\right)^{3/2} \left(\frac{m_i}{m_e}\right)^{1/2}\right]^{-1}. \tag{2.8}$$

On the other hand, the peak growth rates associated with the KCSI are substantial fractions of the lower hybrid frequency as shown in Figure 1a and 2a, and they are assumed to be

$$\frac{\gamma_{KCSI}^M}{\omega_{ce}} = \xi \left(\frac{m_e}{m_i}\right)^{1/2} \qquad \text{where} \quad 0 < \xi < 1. \tag{2.9}$$

We define the value of the parameter ξ as a function of the mass ratio m_i/m_e by the linear interpolation between $m_i/m_e = 100$ and 1836, where the numerical solutions of

the growth rates are obtained in the previous section for the several values of the drift velocity. We set $\xi = 0.4$ at $m_i/m_e = 100$ and $\xi = 0.8$ at $m_i/m_e = 1836$. By equating the peak growth rate of the ECDI with that of the KCSI, that is, $\gamma^M_{ECDI} = \gamma^M_{KCSI}$, we can lead the critical drift velocity as

$$\left(\frac{V_d}{v_e}\right)_{cr} \simeq \left(\frac{T_i}{T_e}\right)\left[\frac{1}{4\xi} - \sqrt{\left(\frac{1}{4\xi}\right)^2 - \frac{2\sqrt{\pi}}{3}\left(\frac{T_i}{T_e}\right)^{1/2}\left(\frac{m_e}{m_i}\right)^{1/2}}\right]. \tag{2.10}$$

If the drift velocity exceeds the critical value given in Equation (2.10), the ECDI will be first destabilized, otherwise the KCSI will be alternatively destabilized. In Figure 3, we show the critical drift velocity normalized by the electron thermal velocity as a function of the mass ratio for the case of $T_i/T_e = 8.0$. The ECDI will be first destabilized in the region represented by red while the KCSI has the larger growth rate in the region shown in blue. The critical drift velocity decreases as the mass ratio increases until approximately $m_i/m_e = 500$. This is because the peak growth rate of the ECDI is almost independent of the mass ratio [*Forslund et al.*, 1972] while that of the KCSI is the substantial fraction of the lower hybrid frequency whose value decreases with increase of the ion mass. When the mass ratio is larger than approximately 500, the critical velocity is almost constant because of increase in ξ.

Chapter 3

Anomalous Electron Heating

In the previous chapter we have shown that the ECDI dominates the KCSI as the electron-ion relative velocity exceeds a critical value which varies according to the mass ratio between an electron and ion, but seems to be a substantial fraction of the electron thermal velocity. In this section we study the electron heating mechanism due to the unstable waves associated with these instabilities, making use of a 2-1/2 dimensional electromagnetic full particle code with the particle-in-cell method (see Appendix B for detailes of this code algorithm). In this code, we assume a doubly periodic boundary in the x and z directions. The numbers of grid points are $N_x \times N_z = 256 \times 512$, and the grid separations are $\Delta x \times \Delta z = 0.1\lambda_e \times 0.1\lambda_e$. The number of particles per grid is 36, so the total number is approximately 5×10^6. The initial values of the plasma parameters are $\omega_{ce}/\omega_{pe} = 0.5$, $T_i/T_e = 8.0$, $m_i/m_e = 100$, and $\beta_i = 1.0$, which are the same as those in the case of Figure 2. The configuration of the uniform magnetic field $\boldsymbol{B}_0$ and the drift velocity $\boldsymbol{V}_d$ is also given in the electron frame as assumed in the previous chapter. We conducted simulations mainly for two cases of the drift velocity; one is $V_d/v_e = 0.8$ where the KCSI is expected to dominate and the other is $V_d/v_e = 2.0$ where the ECDI is expected to dominate.

In Figure 4, we show the time development of the electric field energy for the cases of the two different drift velocities. The total energy and the x, y and z component energies are represented by red, green, yellow, and blue curves, respectively. Figure 4 indicates that the x component of the electric field is overwhelming the other components in both cases while the growth time, in which the total energy of the electric field develops to the saturation level, is much shorter in the case of (b) than (a).

In Figure 5, we present the typical wave spectra in the period during which the amplitude of the unstable waves is growing linearly for the cases of (a) $V_d/v_e = 0.8$ and

(b) $V_d/v_e = 2.0$. The upper panels in both cases are the spectra in the $k_\perp - k_\parallel$ space, and the lower panels are those in the $\omega - k_\perp$ space. Because the x component of the electric field develops dominantly, we use only E_x to evaluate these spectra. Figure 5a indicates that the unstable waves, whose frequencies are approximately the lower hybrid frequency (ω_{lh}), propagate obliquely to the ambient magnetic field. This mode corresponds to the KCSI as expected in the linear analysis. On the other hand, in Figure 5b the characteristic spectra of the KCSI disappears and the ECDI, which propagates perpendicularly to the ambient magnetic field and whose frequencies are a little above the electron cyclotron frequency (ω_{ce}), becomes dominant. Notice that the upper harmonics appear near the upper hybrid frequency (ω_{uh}), nearly the twice of the electron cyclotron frequency in the current parameters. This is because the ECDI is excited by the resonance between the drifting ions and the electron Bernstein waves in the electron frame [*Forslund et al.*, 1970].

3.1 Distribution Function of Electrons

The distribution functions of electrons are shown in Figure 6 at the time when the amplitude of the unstable waves has been saturated (see Figure 4) for the case of the two drift velocities. Figure 6a indicates that electrons are heated parallel to the ambient magnetic field by the unstable waves associated with the KCSI. This is because the obliquely propagating waves due to the KCSI make potential troughs along the magnetic field, and electrons, which are able to move freely in the field-aligned direction, can be easily trapped by the potential troughs [McBride et al., 1972]. On the other hand, Figure 6b shows that electrons are heated perpendicularly to the magnetic field due to the ECDI. In this case, the unstable waves propagate almost perpendicularly to the magnetic field and obliquely propagating waves are weak (see Figure 5b) so that electrons are strong affected by the perpendicularly propagating waves. Since electrons are strongly magnetized, they are not trapped effectively by the potential troughs but some electrons can be trapped in a portion of their cyclotron motions and be accelerated by the waves if the wave amplitudes are enough large. Because the accelerated electrons continue the gyromotion, electrons will be heated isotropically in the x and y directions.

From these results we suggest that the mechanism of an electron heating and the consequent distribution functions depend on the value of the electron-ion relative velocity.

3.2 Heating Level

We next consider how the characteristic temperature of electrons varies according to the electron-ion relative velocity. We define the characteristic temperature as $T_{e\parallel} = m_e\overline{v_{e\parallel}^2}/2$ for the case in which the KCSI is dominant, and $T_{e\perp} = m_e\overline{v_{e\perp}^2}/2$ for the case in which the ECDI is dominant, where $\overline{v_{e\parallel}^2}$ and $\overline{v_{e\perp}^2}$ are the root mean squares of the parallel and perpendicular velocities of electrons, respectively. In Figure 7a we show such characteristic temperature at the time when the amplitude of the unstable waves has been saturated, as a function of the electron-ion relative velocity. The solid line denotes the case where the ECDI is dominant and electrons are perpendicularly heated, and the dashed line represents the case where the KCSI is dominant and electrons are heated parallel to the magnetic field. Figure 7b represents the growth time which is the necessary time for the amplitude of the electric field to have been saturated. We find that the growth time for the case where the ECDI is dominant is very short, compared with that for the case of the KCSI, and seems to be nearly independent of the drift velocity. Figure 7a and 7b indicate that electrons can be rapidly heated by the ECDI up to higher temperature as the drift velocity increases.

The electron heating by the ECDI is possibly caused by the trapping in the potential troughs of the electrostatic waves propagating perpendicularly to the ambient magnetic field, as is mentioned below. The linear growth of the wave amplitude is expected to be slowed when the electron thermal velocity approaches the phase velocity of the electric field V_ϕ and the number of resonant electrons increases. Because the ECDI is excited by the Landau resonance between the drifting ions and the electron Bernstein waves in the electron frame, we can approximate $V_\phi \simeq V_d$. Then the wave amplitudes eventually saturate when the electron thermal velocity reaches the drift velocity. After the trapped electrons are released from the potential troughs, they continue the cyclotron motions so that the distribution function of electrons will be almost isotropic in the $v_x - v_y$ plane. Therefore the electron perpendicular temperature at the time when the wave amplitudes are saturated is expected to be $T_{e,sat}/T_{e,0} = (V_d/v_e)^2$. In other words, electrons can gain energy from the waves by the trapping when $V_d > v_e$. In Figure 8 we show such electron temperature as a function of the drift velocity. The square are the simulation results which are approximated by the dashed line. The solid line represents the above mentioned theoretical prediction. We find that the simulation results are in good agreement with the theory though it is very simple.

We present here, for reference, the detailed heating mechanism suggested by *Chen*

and Birdsall [1973], in which it is described how an electron is trapped by an electrostatic potential trough and accelerated. An electron trapping by an electrostatic wave propagating perpendicularly to a magnetic field is more complex than that in the case there is no magnetic field, because a strongly magnetized electron is likely to make an escape from a potential trough. Consider an electron whose unperturbed gyromotion guiding center is at $x = 0$, and an electrostatic wave propagating perpendicularly (directing to $+x$) to a magnetic field (directing to $+z$). This electron motion satisfies the following equation

$$\frac{dv_x}{dt} = -\frac{e}{m_e}E_x - \omega_{ce}v_y, \tag{3.1}$$

$$\frac{dv_y}{dt} = \omega_{ce}v_x. \tag{3.2}$$

From the combination of Equations (3.1) and (3.2), the total force on the electron in the x direction is

$$F_x = -\frac{\partial}{\partial x}\left[-e\phi(x,t) + \frac{1}{2}m_e\omega_{ce}^2x^2\right] = -\frac{\partial\Phi}{\partial x}, \tag{3.3}$$

where

$$\Phi = -e\phi(x,t) + \frac{1}{2}m_e\omega_{ce}^2x^2. \tag{3.4}$$

$\phi(x,t) = \phi_0\cos(kx - \omega t)$ is a wave potential propagating to the x direction, and ϕ_0 is assumed to be constant. In Equation (3.4) the first term of the right hand side is from the wave potential, on the other hand, the second term represents the magnetic effect and by itself simply describes the gyromotion. A schematic view of wave and particle force potentials in the electron frame are shown in Figure 9 cited from *Chen and Birdsall* [1973]. The black dashed curve is the combined potential Φ. Away from $x = 0$, the relative effect of the wave potential becomes weaker due to the increasing $\boldsymbol{v} \times \boldsymbol{B}_0$ force and, eventually, the combined potential troughs vanish at $|x| = x_v \simeq ek\phi_0/m_e\omega_{ce}^2$, where the wave electric force equals the magnetic force.

Since we consider here the case of $V_d > v_e$, where the ECDI is dominant, the relation between k and r_e is $kr_e < 1$, and from the linear theory we found that the fastest growing wave frequency was approximately the electron cyclotron frequency. These facts indicate that an electron sees at most two troughs during a gyromotion. If the magnetic field is absent, the bounce period is $\tau_b = 2\pi(m_e/ek^2\phi_0)^{1/2}$. There are two conditions for electrons to be effectively trapped by the wave potential troughs in the presence of the magnetic

field. The first is that the time during which an electron sees a single trough, $\tau_1 \sim \lambda/2V_d$, must be longer than τ_b, where λ is the wave length. The second is that the time during which an electron can stay in a traveling trough, $\tau_2 \sim x_v/V_d$, has to be longer than τ_b. If the wave amplitude is large enough as the above conditions are satisfied, electrons will be effectively trapped by wave potential troughs and the model described in Figure 9 is justified.

The model in Figure 9 represents the following scenario. A trapped electron at the point A ($x \lesssim x_v$), which has the total energy (the kinetic energy plus the potential energy) Φ_A, is trapped by the trough and carried to the point B ($x \simeq x_v$) by the traveling wave. At this point, the potential trough vanishes and the electron is released to continue the gyromotion with the total energy $\Phi_B \simeq m_e(\omega_{ce}x_v)^2/2$.

If $T_{e,sat}/T_{e,0} = (V_d/v_e)^2$ is assumed, we can set $\omega_{ce}x_v \simeq V_d$, which gives

$$E_{0,sat} = V_d B_0, \tag{3.5}$$

where $E_{0,sat}$ is the saturation level of the wave amplitude of the fastest growing mode. The comparison between (3.5) and the simulation results is shown in Figure 10. The theoretical prediction in (3.5) well agrees with the simulation results, which justifies the model of Figure 9.

3.3 The Case of Massive Ion with $m_i/m_e = 400$

So far in this chapter, we have considered the case of $m_i/m_e = 100$, where the electron heating occurred perpendicularly to the magnetic field due to the ECDI when $V_d/v_e > 1$ and parallel to the magnetic field due to the KCSI when $V_d/v_e < 1$. We have found that electrons are rapidly heated by the ECDI until the electron thermal velocity reaches the ion bulk velocity in the electron frame. In the case of $m_i/m_e = 100$, the electron heating is due to the fastest growing mode. However the critical drift velocity is below the electron thermal velocity in the case of $m_i/m_e = 1836$, as can be seen in Figures 1(a) and 3. Thus it is possible for the ECDI to be excited even when the drift velocity is under the electron thermal velocity. If electrons are heated by the ECDI in this case, the mechanism can differ from that in the case of $m_i/m_e = 100$, because the upper limit of the electron thermal velocity is the drift velocity in the latter case. Therefore we need to examine how electrons are heated by the ECDI when $V_d < v_e$. Because it is difficult to conduct the full particle simulations for the case of $m_i/m_e = 1836$, with enough resolution, due to

the restriction of the computer resources, we execute the simulations with $m_i/m_e = 400$ in this section.

The time evolution of the wave spectra of E_x in the $k_\perp - k_\parallel$ space is shown in Figure 11, for the case of $V_d/v_e = 0.95$. The ECDI, which has the peak growth rate at $(k_\perp, k_\parallel) = (\pm 6.2, 0.0)$ in this condition, is first excited and rapidly grows during $t\omega_{pe} \lesssim 400$, as is expected from the linear theory. However, it is soon dumped and instead a low wave number (viz. a low frequency) mode, the KCSI, becomes dominant after $t\omega_{pe} \simeq 480$. In Figure 12, we present the electron distribution functions at the corresponding time to the wave spectra in Figure 11. It is interesting that electrons are not heated effectively, although the ECDI is dominant until $t\omega_{pe} \simeq 400$. This is because a lot of electrons can be resonant with the electrostatic waves in the case of $V_d/v_e < 1$, as a result, the unstable waves are attenuated before they have grown large enough to effectively trap electrons. Indeed a low saturation level is also deduced from Figure 10 in the case of $V_d/v_e < 1$. Since the KCSI is dominant after $t\omega_{pe} \gtrsim 480$, electrons are eventually heated parallel to the ambient magnetic field.

Chapter 4

Discussion

4.1 Travel Time and Growth Time

So far we have assumed that electrons are strongly magnetized while ions are unmagnetized. However this assumption is valid only inside the diffusion region, which spreads from the X-type neutral line with the order of the ion inertial length λ_i in the z direction and $10\lambda_i$ in the x direction [e.g., *Shay et al.*, 1998]. Since ions outside the diffusion region are also expected to be magnetized, the relative velocity between electrons and ions nearly disappears, stabilizing both the ECDI and the KCSI. It is therefore important to check whether there is enough time for the unstable waves to be saturated and heat electrons up to the level described in Figure 7a while electrons are passing through the diffusion region. In Figure 13 we represent the growth time (which is the simulation result) of the most unstable wave associated with the ECDI (solid line) and the KCSI (dashed line), which are the same as those in Figure 7b, and the travel time of electrons drifting across the diffusion region (thick solid curve), as a function of the drift velocity. We estimated the travel time as roughly $10\lambda_i/V_d$, using the same parameters with those in the simulation. The travel time may be underestimated because the relative electron-ion velocity V_d becomes lower during the passage. Figure 13 indicates that the travel time is greater than the growth time for all points, so that there is enough time for the two unstable modes to be saturated and heat the electrons up to the level shown in Figure 7a.

4.2 Comparison with Observations

The instabilities associated with a cross-field relative motion between electrons and ions vary according to the relative magnitude of the relative electron-ion velocity to the initial thermal velocity of electrons. Here we compare the magnitude of the electron drift velocity, assuming that ions have no bulk velocity, with that of the electron thermal velocity inferred from observational results and examine which mode is expected to be excited in the reconnection region formed in the Earth magnetotail. Since the upper limit of the outflowing electron drift velocity just outside the electron diffusion region is expected to be the electron Alfvén velocity V_{Ae} in the inflow region [e.g., *Shay et al.*, 2001; *Hoshino et al.*, 2001] as already mentioned, we assume the relative electron-ion velocity V_d is equivalent to V_{Ae}. Thus we compare the electron thermal velocity v_e with the electron Alfvén velocity V_{Ae} so as to determine which unstable mode and the resultant electron heating is operative.

In order to calculate the electron Alfvén velocity we assume $B_L = (B_x^2 + B_y^2)^{1/2} = 15$ nT and $n_{ps} \approx 0.3\,\mathrm{cm}^{-3}$ after *Baumjohann et al.* [1989] and obtain $V_{Ae}/c \approx 0.085$. On the other hand, to estimate the electron thermal velocity in the plasma sheet at the time of the reconnection, we use, for example, the observational data presented by *Shinohara et al.* [1998] (see Table 1, therein), which were obtained by Geotail observation. Though their data were probably taken outside the diffusion region because they observed fast tailward ion flows with southward B_z at the same time, we assume that the plasma parameter necessary for calculating of the electron thermal velocity, that is, the electron temperature is almost common around the diffusion region. From their data we obtain several values ranging from $v_e/c = 0.066$ ($T_e = 1.1$ keV) to $v_e/c = 0.119$ ($T_e = 3.6$ keV) (see Figure 14). Since the linear theory represents that the critical drift velocity, where the growth rate of the ECDI exceeds that of the KCSI, is approximately $0.6v_e$ (see Figure 1a), the electron Alfvén velocity seems to exceed the critical value for any case so that the ECDI is expected to be excited. However the electron heating associated with the ECDI is weak for the case of $V_d/v_e < 1$, as mentioned in Section 3.3. Thus the electron heating by the KCSI will dominate in the case of $V_d/v_e < 1$ even though the growth rate of the KCSI is lower than that of the ECDI. Therefore we can expect that both modes are possible to be excited and heat electrons in parallel or perpendicular to the ambient magnetic field.

As for the identification of the excited mode through an analysis of the wave data obtained by spacecraft observations, the frequency of excited wave is quite helpful. The

real frequencies of the KCSI with the maximum growth rate for the various drift velocities can be read from Figure 1 to range from $0.04\,\omega_{pe}$ to $0.11\,\omega_{pe}$. The wave numbers ($k_\perp$) corresponding to these cases can be evaluated to range from $1.01\,\lambda_e^{-1}$ to $0.93\,\lambda_e^{-1}$. Therefore the Doppler-shifted frequencies ($\omega_r - k_\perp v$) are in the range from $-0.011\,\omega_{pe}$ to $-0.010\,\omega_{pe}$ (see Figure 15), where we assume that the observation will be made in the ion frame and take $v = V_d$. In the same way, the Doppler-shifted frequencies of the waves excited by the ECDI take the values from $-0.062\,\omega_{pe}$ to $-0.039\,\omega_{pe}$, where the values of ω_r and $k_\perp$ range from $0.545\,\omega_{pe}$ to $0.678\,\omega_{pe}$, and $12.14\,\lambda_e^{-1}$ to $5.74\,\lambda_e^{-1}$, respectively. Thus for the observed waves which have the frequencies near the the lower hybrid frequency ($\omega_{lh} = 0.012\,\omega_{pe}$ in Figure 1), we can assume that they are excite by the KCSI. On the other hand, for the waves which have lower frequencies around $0.05\,\omega_{pe}$, it can be assumed that they are excited by the ECDI.

Chapter 5

Summary and Conclusion

In this paper, we examined a possible mechanism of an electron heating due to a strong Hall current, which is caused by a large velocity difference between electrons and ions inside the diffusion region. We first solved the linear kinetic dispersion relation in order to identify possible instabilities. We found that the unstable mode varied according to the electron-ion relative velocity. In the case of the real mass ratio, $m_i/m_e = 1836$, the fastest growing mode is the high frequency mode associated with the ECDI when $V_d/v_e \gtrsim 0.6$, while it is the low frequency mode associated with the KCSI when $V_d/v_e \lesssim 0.6$. However the critical value of the drift velocity, where the sort of the most unstable mode changes, increases as the mass ratio decreases. This is because the growth rate of the ECDI is almost independent of the mass ratio, different from that of the KCSI, which decreases as the mass ratio increases since the value is the substantial fraction of the lower hybrid frequency. This is the character worth attention when we conduct a numerical simulation, in which it is usually difficult to use the real mass ratio because of the restriction of the computer resources.

We next conducted the 2-1/2 dimensional electromagnetic full particle simulations to examine the electron heating due to the unstable waves. We found that electrons are heated perpendicularly to the ambient magnetic field due to the ECDI, while the heating is in the parallel direction by the KCSI. In particular, we showed that electrons could be very quickly heated up to $v_e \simeq V_d$ by the trapping in the electrostatic potential troughs, when the ECDI was dominant. We also showed that the electron heating associated with the ECDI could be, however, ineffective when $V_d/v_e < 1$ even though the ECDI is first excited. This is because the number of resonant electrons is so large when $V_d/v_e < 1$ that the wave amplitude is saturated at low level and soon dumped before it grows large enough to trap electrons effectively. It is important that the most dominant instability

and the resultant mechanism of an electron heating vary around $V_d/v_e = 1.0$, because the electron thermal velocity may be comparable with the electron-ion relative velocity inside the diffusion region according to the satellite observations. The identification of the dominant unstable mode will be possible by an analysis of the wave data obtained by spacecraft observations, since the frequency ranges of the KCSI and the ECDI are different; the former is nearly the lower hybrid frequency while the latter is around $|\omega'| = 0.05\omega_{pe}$, higher than the former. The Buneman-type instability is not necessarily excited because this instability is a magnetohydrodynamic limit of the ECDI and seems to be dominant when $V_d/v_e >> 1$.

Because we have concentrated our attention only on a local region inside the diffusion region with high spatial and time resolution, we cannot discuss the dynamics around the diffusion region, including the feedback effects of the electron heating to the diffusion region. In order to understand the self-consistent mechanism of the magnetic reconnection including Hall effects near the X-type neutral line, we need to conduct a simulation that covers more extensive region with high spatial and time resolution especially in the diffusion region.

Acknowledgments

The author would like to express grateful appreciation to Prof. S. Machida for his illuminating guidance and discussion. The author also wishes to thank Prof. T. Araki, Prof. T. Iyemori, Mr. T. Kamei, Dr. M. Takeda, Dr. A. Saito, and Dr. M. Nosé for their helpful comments and discussions. The author is grateful to Drs A. Yajima, N. Terada, Y. Miyashita, and all colleagues of Department of Geophysics, Kyoto University for their valuable instruction and technical support. The author finally would like to thank Prof. S. Fujita of Meteorological College for his encouragement. Without his guidance to the space physics, this work would not have been taken up and, of course, accomplished.

Appendix A

Derivation of the Kinetic Plasma Dispersion Relation

In this Appendix we derive a kinetic plasma dispersion relation, including oblique propagation of unstable waves and the electron cyclotron resonance, when the unperturbed distribution functions of electrons and ions are defined as Equations (2.1) and (2.2), respectively. We assume wave frequencies are much higher than the ion cyclotron frequency so that ions are unmagnetized while electrons still remain frozen-in to the ambient magnetic field.

A.1 Perturbed Distribution Function δf

We follow the method described in *Nicholson* [1983] in order to derive the general form of the perturbed distribution function. The fundamental equation is the Vlasov equation,

$$\frac{\partial f_s}{\partial t} + \boldsymbol{v} \cdot \nabla_{\boldsymbol{x}} f_s + \frac{q_s}{m_s} (\boldsymbol{E} + \boldsymbol{v} \times \boldsymbol{B}) \cdot \nabla_{\boldsymbol{v}} f_s = 0, \tag{A.1}$$

where suffix s denotes the particle species (electron or ion). In order to linearize Equation (A.1) around the unperturbed distribution function, we put

$$\begin{aligned} f_s(\boldsymbol{x}, \boldsymbol{v}, t) &= f_{s0}(\boldsymbol{v}) + \delta f_s(\boldsymbol{x}, \boldsymbol{v}, t), \\ \boldsymbol{E}(\boldsymbol{x}, t) &= \delta \boldsymbol{E}(\boldsymbol{x}, t), \\ \boldsymbol{B}(\boldsymbol{x}, t) &= \boldsymbol{B}_0 + \delta \boldsymbol{B}(\boldsymbol{x}, t). \end{aligned}$$

Notice that we study in the electron frame so that the uniform electric field is zero. Then the linearized Vlasov equation for species s is

$$\frac{d\delta f_s}{dt} = -\frac{q_s}{m_s}\left(\delta \boldsymbol{E} + \boldsymbol{v} \times \delta \boldsymbol{B}\right) \cdot \nabla_{\boldsymbol{v}} f_{s0}, \tag{A.2}$$

where $d/dt = \partial_t + \boldsymbol{v} \cdot \nabla_{\boldsymbol{x}} + q_s/m_s(\boldsymbol{v} \times \boldsymbol{B}_0) \cdot \nabla_{\boldsymbol{v}}$ is the total differential along the unperturbed orbits of particles in the phase space. Therefore in order to derive the unperturbed distribution function both sides of Equation (A.2) are integrated along the unperturbed orbits. We pursue the unperturbed orbit $(\boldsymbol{X}(t), \boldsymbol{V}(t))$ of a particle whose motion is controled by Newton's low of motion in the real space. The governing equations of a particle motion on this orbit are

$$\frac{d\boldsymbol{X}(t)}{dt} = \boldsymbol{V}(t), \tag{A.3}$$

and

$$\frac{d\boldsymbol{V}(t)}{dt} = \frac{q_s}{m_s}\boldsymbol{V}(t) \times \boldsymbol{B}_0[\boldsymbol{X}(t), t]. \tag{A.4}$$

From Equations (A.3) and (A.4), we know that the unperturbed orbit can be given by the following form,

$$\begin{aligned} \boldsymbol{X}(t') &= \boldsymbol{x} - \int_{t'}^{t} \frac{d\boldsymbol{X}(t'')}{dt''}\, dt'', \\ \boldsymbol{V}(t') &= \boldsymbol{v} - \int_{t'}^{t} \frac{d\boldsymbol{V}(t'')}{dt''}\, dt'', \end{aligned} \tag{A.5}$$

where the integral constants are determined as they satisfy the relations $\boldsymbol{X}(t) = \boldsymbol{x}$ and $\boldsymbol{V}(t) = \boldsymbol{v}$. As a result the orbit $(\boldsymbol{X}(t'), \boldsymbol{V}(t'))$ represents that of a particle which approach the point $(\boldsymbol{x}, \boldsymbol{v})$ at time t. Here we define a particle position in the phase space $(\boldsymbol{x}', \boldsymbol{v}')$ as $\boldsymbol{x}' = \boldsymbol{X}(t')$ and $\boldsymbol{v}' = \boldsymbol{V}(t')$, which mean that the particle on the orbit $(\boldsymbol{X}(t'), \boldsymbol{V}(t'))$ is located at the position $(\boldsymbol{x}', \boldsymbol{v}')$ at time t'. (Notice that capital letters $(\boldsymbol{X}, \boldsymbol{V})$ represent an orbit curve as a function of time t in the seven-dimensional phase space while small letters $(\boldsymbol{x}, \boldsymbol{v})$ denotes the particle position on the orbit at particular time.) Then we rewrite Equation (A.1) as

$$\frac{d}{dt'}\delta f_s(\boldsymbol{x}', \boldsymbol{v}', t') = -\frac{q_s}{m_s}[\delta \boldsymbol{E}(\boldsymbol{x}', t') + \boldsymbol{v}' \times \delta \boldsymbol{B}(\boldsymbol{x}', t')] \cdot \nabla_{\boldsymbol{v}'} f_{s0}(\boldsymbol{v}'). \tag{A.6}$$

Integrating both sides of Equation (A.6) from $t' = -\infty$ to $t' = t$, we can obtain

$$\delta f_s(\boldsymbol{x}, \boldsymbol{v}, t) = \delta f_s(\boldsymbol{x}', \boldsymbol{v}', t' = -\infty) - \frac{q_s}{m_s}\int_{-\infty}^{t} dt' \left[\delta \boldsymbol{E}(\boldsymbol{x}', t') + \boldsymbol{v}' \times \delta \boldsymbol{B}(\boldsymbol{x}', t')\right] \cdot \nabla_{\boldsymbol{v}'} f_{s0}(\boldsymbol{v}'). \tag{A.7}$$

Equation (A.7) is a general form of the perturbed distribution function. In the following, we calculate the wave form solution of Equation (A.7), assuming

$$\begin{aligned}
\delta\boldsymbol{E}(\boldsymbol{x},t) &= \delta\hat{\boldsymbol{E}}\exp[i(\boldsymbol{k}\cdot\boldsymbol{x}-\omega t)],\\
\delta\boldsymbol{B}(\boldsymbol{x},t) &= \delta\hat{\boldsymbol{B}}\exp[i(\boldsymbol{k}\cdot\boldsymbol{x}-\omega t)],\\
\delta\boldsymbol{f}_s(\boldsymbol{x},\boldsymbol{v},t),&= \delta\hat{\boldsymbol{f}}_s(\boldsymbol{v})\exp[i(\boldsymbol{k}\cdot\boldsymbol{x}-\omega t)],
\end{aligned} \tag{A.8}$$

where $\delta\hat{\boldsymbol{E}}$ and $\delta\hat{\boldsymbol{B}}$ are constant vectors, $\boldsymbol{k} = k_\perp\hat{\boldsymbol{e}}_x + k_\parallel\hat{\boldsymbol{e}}_z$, and $\omega = \omega_r + i\gamma$. Since we are here only interested in unstable waves with positive growth rates, we set the initial fluctuation $\delta f_s(t' = -\infty)$ to be zero, which allow us to neglect the first term in the right hand side of Equation (A.7). Thus Equation (A.7) is manipulated into the following form,

$$\delta\hat{f}_s = -\frac{q_s}{m_s}\int_{-\infty}^{0} d\tau[\delta\hat{\boldsymbol{E}} + \boldsymbol{v}'\times\delta\hat{\boldsymbol{B}}]\cdot\nabla_{\boldsymbol{v}'}f_{s0}(\boldsymbol{v}')\exp[i(\boldsymbol{k}\cdot\boldsymbol{\xi}-\omega\tau)], \tag{A.9}$$

where $\boldsymbol{\xi} = \boldsymbol{x}' - \boldsymbol{x}$ and $\tau = t' - t$, and the position $(\boldsymbol{x}', \boldsymbol{v}')$ is put on the orbit $(\boldsymbol{X}(\tau), \boldsymbol{V}(\tau))$ which passes the point $(\boldsymbol{x}, \boldsymbol{v})$ at $\tau = 0$.

A.1.1 Ion Contribution

Since we assume that ions are unmagnetized, the unperturbed orbits of ions are calculated from Equations (A.3) and (A.4) with $\boldsymbol{B}_0 = 0$ as

$$\boldsymbol{V}(t') = \boldsymbol{v}, \qquad \boldsymbol{X}(t') = \boldsymbol{x} + \boldsymbol{v}\tau.$$

Since $\boldsymbol{v}'$ is independent of τ, it is easy to execute the integration in Equation (A.9) and we obtain

$$\delta\hat{f}_i = \frac{e}{m_i}\frac{\delta\hat{\boldsymbol{E}}}{i(\omega - \boldsymbol{k}\cdot\boldsymbol{v})}\cdot\nabla_{\boldsymbol{v}}f_{i0}, \tag{A.10}$$

where we put $\delta\hat{\boldsymbol{B}} = 0$ because of the assumption of unmagnetization. Making use of the isotropic nature of the unperturbed distribution function in the velocity space, we can manipulate Equation (A.10) into the following form,

$$\delta\hat{f}_i = i\frac{2e}{m_i}\frac{(v_x - V_d)\delta\hat{E}_x + v_y\delta\hat{E}_y + v_z\delta\hat{E}_z}{\boldsymbol{k}\cdot\boldsymbol{v} - \omega}\frac{\partial f_{i0}}{\partial v_\perp^2}, \tag{A.11}$$

where $v_\perp^2 = (v_x - V_d)^2 + v_y^2$.

A.1.2 Electron Contribution

Electrons conduct the cyclotron motion around the magnetic field line. From Equations (A.3) and (A.4) we derive the unperturbed orbits of electrons as

$$\begin{aligned}
V_x(\tau) &= v_\perp \cos(\omega_{ce}(t'-t)+\theta) = v_\perp \cos(\omega_{ce}\tau+\theta),\\
V_y(\tau) &= v_\perp \sin(\omega_{ce}(t'-t)+\theta) = v_\perp \sin(\omega_{ce}\tau+\theta),\\
V_z(\tau) &= v_\parallel,\\
X(\tau) &= x + \frac{v_\perp}{\omega_{ce}}[\sin(\omega_{ce}\tau+\theta)-\sin\theta],\\
Y(\tau) &= y - \frac{v_\perp}{\omega_{ce}}[\cos(\omega_{ce}\tau+\theta)-\cos\theta],\\
Z(\tau) &= z + v_\parallel \tau,
\end{aligned} \tag{A.12}$$

where $v_\parallel = v_z$, and θ $(0 \le \theta \le 2\pi)$ is the initial phase at $\tau = 0$ in the velocity space. In this case, since $\boldsymbol{v}'$ is a function of τ the execution of the integration in Equation (A.9) is slightly complicated. We eliminate $\delta\hat{\boldsymbol{B}}$ from Equation (A.9) by using Faraday's low and substitute (A.12) into the resultant equation. After some algebraic calculation we obtain

$$\delta\hat{f}_e = i\frac{2e}{m_e}\sum_{n=-\infty}^{\infty}\frac{\frac{n}{\lambda}v_\perp J_n\delta\hat{E}_x + iv_\perp J_n'\delta\hat{E}_y + v_\parallel J_n\delta\hat{E}_z}{\omega - n\omega_{ce} - k_\parallel v_\parallel}\frac{\partial f_{e0}}{\partial v_\perp^2}\exp[n(\theta-\frac{\pi}{2})+\lambda\cos\theta], \tag{A.13}$$

where $\lambda = k_\perp v_\perp/\omega_{ce}$, $J_n = J_n(\lambda)$ is the Bessel function of order n, and $J_n' = dJ_n(\lambda)/d\lambda$. In deriving Equation (A.13) we used the following identical equation,

$$e^{i\lambda\sin\theta} = \sum_{n=-\infty}^{\infty} J_n(\lambda)\exp[in\theta], \tag{A.14}$$

and the differential form of (A.14) about λ and θ,

$$e^{i\lambda\sin\theta}\sin\theta = -i\sum_{n=-\infty}^{\infty} J_n' e^{in\theta}, \quad e^{i\lambda\sin\theta}\cos\theta\sum_{n=-\infty}^{\infty}\frac{n}{\lambda}J_n e^{in\theta}.$$

A.2 Dispersion Relation

In order to complete the linearize equation system which gives the linear dispersion relation, we here introduce Maxwell's equations. We assume the wave form solutions given in (A.8) and replace $\partial/\partial t$ with $-i\omega$ and ∇ with $i\boldsymbol{k}$. Then Faraday's law and

Ampère's law are expressed like

$$\delta\hat{\boldsymbol{B}} = \frac{\boldsymbol{k}\times\delta\hat{\boldsymbol{E}}}{\omega}, \tag{A.15}$$

$$i\boldsymbol{k}\times\delta\hat{\boldsymbol{B}} = \mu_0\,\delta\hat{\boldsymbol{j}} - i\frac{\omega}{c^2}\,\delta\hat{\boldsymbol{E}}, \tag{A.16}$$

where $\delta\hat{\boldsymbol{j}}$ is the Fourier component of the fluctuating current density $\delta\boldsymbol{j}$. $\delta\hat{\boldsymbol{j}}$ is defined by

$$\delta\hat{\boldsymbol{j}} = e\left[\int \boldsymbol{v}\delta\hat{f}_i\,d^3v - \int \boldsymbol{v}\delta\hat{f}_e\,d^3v\right]. \tag{A.17}$$

Substituting Equations (A.11) and (A.13) into (A.17) and executing the integration over the velocity space, we can derive $\delta\boldsymbol{j}$ and the dielectric tensor by combining it with Equations (A.15) and (A.16). On calculation of the integration in (A.17) we use the following relations,

$$\int_0^\infty xJ_n^2(\alpha x)\,e^{-x^2}dx = \frac{1}{2}I_n(\alpha^2/2)\,e^{-\alpha^2/2},$$

$$\int_0^\infty x^2J_n'(\alpha x)J_n(\alpha x)\,e^{-x^2}dx = \frac{\alpha}{4}[I_n'(\alpha^2/2) - I_n(\alpha^2/2)]\,e^{-\alpha^2/2},$$

$$\int_0^\infty x^3[J_n'(\alpha x)]^2\,e^{-x^2}dx = \left[\left(\frac{n^2}{2\alpha^2}+\frac{\alpha^2}{4}\right)I_n(\alpha^2/2) - \frac{\alpha^2}{4}I_n'(\alpha^2/2)\right]\,e^{-\alpha^2/2},$$

where $I_n(x)$ is the modified Bessel function of order n, and $I_n'(x) = dI_n(x)/dx$. After some calculation we obtain

$$\delta\hat{\boldsymbol{j}} = \boldsymbol{\sigma}\cdot\delta\hat{\boldsymbol{E}}, \tag{A.18}$$

where $\boldsymbol{\sigma}$ is the conductivity tensor and the elements are expressed by the following form,

$$\sigma_{xx} = -i\,\frac{2\varepsilon\omega_{pi}^2}{k^2v_i^2}\omega[1+\xi_iZ(\xi_i)]\sin^2\theta - i\,\frac{\varepsilon_0\omega_{pe}^2}{\omega}\frac{e^{-\mu}}{\mu}\sum_{n=-\infty}^{\infty}n^2I_n\xi_0Z(\xi_n),$$

$$\sigma_{yy} = -i\frac{2\varepsilon\omega_{pe}^2}{\omega}\mu e^{-\mu}\sum_{n=-\infty}^{\infty}\left\{\frac{n^2}{2\mu^2}I_n + (I_n - I_n')\right\}\xi_0Z(\xi_n),$$

$$\sigma_{zz} = -i\frac{2\varepsilon_0\omega_{pi}^2}{k^2v_i^2}\omega[1+\xi_iZ(\xi_i)]\cos^2\theta - i\frac{2\varepsilon_0\omega_{pi}^2}{\omega}e^{-\mu}\sum_{n=-\infty}^{\infty}I_n\xi_0\xi_n[1+\xi_nZ(\xi_n)],$$

$$\sigma_{xy} = -\sigma_{yx} = \frac{\varepsilon_0\omega_{pe}^2}{\omega}e^{-\mu}\sum_{n=-\infty}^{\infty}n(I_n' - I_n)\xi_0Z(\xi_n),$$

$$\sigma_{xz} = \sigma_{zx} = -i\frac{2\varepsilon_0\omega_{pi}^2}{k^2v_i^2}\omega[1+\xi_iZ(\xi_i)]\sin\theta\cos\theta - i\frac{\varepsilon_0\omega_{pe}^2}{\omega}\sqrt{\frac{2}{\mu}}e^{-\mu}\sum_{n=-\infty}^{\infty}nI_n\xi_0[1+\xi_nZ(\xi_n)],$$

$$\sigma_{yz} = -\sigma_{zy} = -\frac{\varepsilon_0\omega_{pe}^2}{\omega}\sqrt{2\mu}e^{-\mu}\sum_{n=-\infty}^{\infty}(I_n' - I_n)\xi_0[1+\xi_nZ(\xi_n)],$$

where $\xi_n = (\omega - n\omega_{ce})/k_\parallel v_e$, $\mu = k_\perp^2 v_e^2/2\omega_{ce}^2$, $\xi_i = (\omega - k_\perp V_d)/kv_i$, $\theta = \tan^{-1}(k_\perp/k_\parallel)$, and $Z(\xi)$ is the plasma dispersion function [*Fried and Conte*, 1961]. We substitute (A.18) into Equation (A.16) and use Equation (A.15) to eliminate $\delta\hat{\boldsymbol{B}}$. Then (A.16) is reduced into

$$\begin{pmatrix} D_{xx} & D_{xy} & D_{xz} \\ D_{yx} & D_{yy} & D_{yz} \\ D_{zx} & D_{zy} & D_{zz} \end{pmatrix} \begin{pmatrix} \delta\hat{E}_x \\ \delta\hat{E}_y \\ \delta\hat{E}_z \end{pmatrix} = 0, \tag{A.19}$$

where

$$\begin{aligned}
D_{xx} &= 1 - \frac{c^2k^2}{\omega^2}\cos^2\theta + \frac{2\omega_{pi}^2}{k^2v_i^2}[1 + \xi_i Z(\xi_i)]\sin^2\theta + \frac{\omega_{pe}^2}{\omega^2}\frac{e^{-\mu}}{\mu}\sum_{n=-\infty}^{\infty} n^2 I_n \xi_0 Z(\xi_n), \\
D_{yy} &= 1 - \frac{c^2k^2}{\omega^2} + \frac{2\omega_{pe}^2}{\omega^2}\mu e^{-\mu}\sum_{n=-\infty}^{\infty}\left\{\frac{n^2}{2\mu^2}I_n + (I_n - I_n')\right\}\xi_0 Z(\xi_n), \\
D_{zz} &= 1 - \frac{c^2k^2}{\omega^2}\sin^2\theta + \frac{2\omega_{pi}^2}{k^2v_i^2}[1 + \xi_i Z(\xi_i)]\cos^2\theta + \frac{2\omega_{pe}^2}{\omega^2}e^{-\mu}\sum_{n=-\infty}^{\infty} I_n\xi_0\xi_n[1 + \xi_n Z(\xi_n)], \\
D_{xy} &= -D_{yx} = -i\frac{\omega_{pe}^2}{\omega^2}e^{-\mu}\sum_{n=-\infty}^{\infty} n(I_n - I_n')\xi_0 Z(\xi_n), \\
D_{xz} &= D_{zx} = \frac{c^2k^2}{\omega^2}\sin\theta\cos\theta + \frac{2\omega_{pi}^2}{k^2v_i^2}[1 + \xi_i Z(\xi_i)]\sin\theta\cos\theta + \frac{\omega_{pe}^2}{\omega^2}\sqrt{\frac{2}{\mu}}e^{-\mu}\sum_{n=-\infty}^{\infty} nI_n\xi_0[1 + \xi_n Z(\xi_n)], \\
D_{yz} &= -D_{zy} = i\frac{\omega_{pe}^2}{\omega^2}\sqrt{2\mu}e^{-\mu}\sum_{n=-\infty}^{\infty}(I_n - I_n')\xi_0[1 + \xi_n Z(\xi_n)].
\end{aligned} \tag{A.20}$$

The kinetic dispersion relation is defined by $\det[\boldsymbol{D}] = 0$.

In order to facilitate the discussion about the electrostatic and electromagnetic effects in the dispersion relation, we next derive the dispersion tensor $\boldsymbol{D}$ in a representation based on the scalar and vector potentials $\delta\hat{\phi}$, $\delta\hat{\boldsymbol{A}}$, rather than the electric field $\delta\hat{\boldsymbol{E}}$, after *Tsai et al.*, [1984]. Since $\delta\hat{\boldsymbol{E}} = -i\boldsymbol{k}\delta\hat{\phi} + i\omega\delta\hat{\boldsymbol{A}}$ and $\boldsymbol{k}\cdot\delta\hat{\boldsymbol{A}} = 0$ (Coulomb gauge), we can write

$$\begin{pmatrix} \delta\hat{E}_x \\ \delta\hat{E}_y \\ \delta\hat{E}_z \end{pmatrix} = i\omega \begin{pmatrix} -\frac{k_\perp}{k} & 0 & -\frac{k_\parallel}{k_\perp} \\ 0 & 1 & 0 \\ -\frac{k_\parallel}{k} & 0 & 1 \end{pmatrix} \begin{pmatrix} \frac{k}{\omega}\delta\hat{\phi} \\ \delta\hat{A}_y \\ \delta\hat{A}_z \end{pmatrix}. \tag{A.21}$$

Using the potential representations, we can rewrite Equation (A.19) as

$$\begin{pmatrix} D_{11} & D_{12} & D_{13} \\ D_{21} & D_{22} & D_{23} \\ D_{31} & D_{32} & D_{33} \end{pmatrix} \begin{pmatrix} k/\omega\delta\hat{\phi} \\ \delta\hat{A}_y \\ \delta\hat{A}_z \end{pmatrix} = 0. \tag{A.22}$$

From Equations (A.19), (A.21) and (A.22), we can show that

$$
\begin{aligned}
D_{11} &= \frac{k_\perp^2}{k^2} D_{xx} + \frac{2k_\perp k_\parallel}{k^2} D_{xz} + \frac{k_\parallel}{k^2} D_{zz}, \\
D_{22} &= D_{yy}, \\
D_{33} &= \frac{k_\parallel^2}{k^2} D_{xx} - \frac{2k_\perp k_\parallel}{k^2} D_{xz} + \frac{k_\perp^2}{k^2} D_{zz}, \\
D_{12} &= -D_{21} = -\frac{k_\perp}{k} D_{xy} + \frac{k_\parallel}{k} D_{yz}, \\
D_{13} &= \frac{k^2}{k_\perp^2} D_{31} = \frac{k_\parallel}{k} D_{xx} - \frac{k_\perp^2 - k_\parallel^2}{k k_\perp} D_{xz} - \frac{k_\parallel}{k} D_{zz}, \\
D_{23} &= -\frac{k^2}{k_\perp^2} D_{32} = \frac{k_\parallel}{k_\perp} D_{xy} + D_{yz}.
\end{aligned} \tag{A.23}
$$

The representation of (2.5) can be obtained by substituting (A.20) into (A.23). In the $\delta\hat{\phi}$, $\delta\hat{\boldsymbol{A}}$ representation, the dispersion relation reduces to $D_{11} = 0$ if electromagnetic effect is ignored.

Appendix B

Algorithm in the Full Particle Code

In a usual plasma particle simulation, we employ modeled particle called *superparticles*, which has a finite spatial scale about the order of the spatial grid size. This is because we need to simulate with far fewer particles than in a real case. For example, provided that plasma includes electrons with number density $1.0\,/cc$ and thermal velocity c (the light velocity), the Debye length is $\lambda_D \approx 10^5\,m$. If we set the grid separations to be $\lambda_D/10$, the number of particles par grid is approximately 10^{12} for a two-dimensional simulation. Overall the simulation space with 100×100 grids, it is above 10^{16} that is necessary number of particles to conduct a simulation. It is totally impossible to treat such a vast number of particles. Furthermore, the *superparticles* with broad shapes are beneficial to moderate numerical noises. In this appendix, we show the detailed algorithm in our 2-1/2 dimensional full particle simulation code with the *superparticles* [*Birdsall and Langdon*, 1995].

B.1 Fundamental Equations

The position $\boldsymbol{x}_{sj}$ and the velocity $\boldsymbol{v}_{sj}$ of the j-th particle obey Newton's law,

$$m_s \frac{d\boldsymbol{v}_{sj}}{dt} = q_s \left[\boldsymbol{E}(\boldsymbol{x}_{sj}) + \boldsymbol{v}_{sj} \times \boldsymbol{B}(\boldsymbol{x}_{sj})\right], \tag{B.1}$$

$$\frac{d\boldsymbol{x}_{sj}}{dt} = \boldsymbol{v}_{sj}, \tag{B.2}$$

where m_s and q_s represent the mass and the charge of a particle (a *superparticle*) of species s, respectively. The electromagnetic field is described by Maxwell's equations,

$$\frac{\partial \boldsymbol{B}}{\partial t} = -\nabla \times \boldsymbol{E}, \tag{B.3}$$

$$\frac{1}{c^2}\frac{\partial \boldsymbol{E}}{\partial t} = \nabla \times \boldsymbol{B} - \mu_0 \boldsymbol{j}, \tag{B.4}$$

$$\nabla \cdot \boldsymbol{E} = \frac{\rho}{\varepsilon_0}, \tag{B.5}$$

$$\nabla \cdot \boldsymbol{B} = 0, \tag{B.6}$$

where the charge density ρ and the current density $\boldsymbol{j}$ is defined at each grid $\boldsymbol{X}_i$,

$$\rho(\boldsymbol{X}_i) = \sum_s q_s n_s(\boldsymbol{X}_i), \tag{B.7}$$

$$\boldsymbol{j}(\boldsymbol{X}_i) = \sum_s q_s n_s(\boldsymbol{X}_i)\boldsymbol{v}_s, \tag{B.8}$$

where n_s is the number density.

In order to normalize Equations from (B.1) to (B.8), we put the normalized quantities in the following forms,

$$\begin{aligned}
&m_s^* = \frac{m_s}{m_e}, \quad \boldsymbol{x}_s^* = \frac{\omega_{pe}}{c}\boldsymbol{x}_s, \quad t^* = \omega_{pe}t, \quad q_s^* = \frac{q_s}{e} \\
&\boldsymbol{v}_s^* = \frac{\boldsymbol{v}_s}{c}, \quad \omega^* = \frac{\omega}{\omega_{pe}}, \quad \boldsymbol{E}^* = \frac{e\boldsymbol{E}}{m_e c\omega_{pe}}, \\
&\boldsymbol{B}^* = \frac{e\boldsymbol{B}}{m_e\omega_{pe}}, \quad \rho^* = \frac{1}{e}\left(\frac{c}{\omega_{pe}}\right)^2 \rho, \quad \boldsymbol{j}^* = \frac{1}{ec}\left(\frac{c}{\omega_{pe}}\right)^2 \boldsymbol{j}, \\
&n_s^* = \left(\frac{c}{\omega_{pe}}\right)^2 n_s,
\end{aligned} \tag{B.9}$$

where the asterisk denotes that the quantities are dimensionless. Using (B.9), We can rewrite the fundamental equations as the following forms.
Newton's law,

$$m_s^* \frac{d\boldsymbol{v}_{sj}^*}{dt^*} = q_s^* \left[\boldsymbol{E}^*(\boldsymbol{x}_{sj}^*) + \boldsymbol{v}_{sj}^* \times \boldsymbol{B}^*(\boldsymbol{x}_{sj}^*)\right], \tag{B.10}$$

$$\frac{d\boldsymbol{x}_{sj}^*}{dt^*} = \boldsymbol{v}_{sj}^*, \tag{B.11}$$

Maxwell's equations,

$$\frac{\partial \boldsymbol{B}^*}{\partial t^*} = -\nabla^* \times \boldsymbol{E}^*, \tag{B.12}$$

$$\frac{\partial \boldsymbol{E}^*}{\partial t^*} = \nabla^* \times \boldsymbol{B}^* - \frac{1}{n_0^*}\boldsymbol{j}^*, \tag{B.13}$$

$$\nabla^* \cdot \boldsymbol{E}^* = \frac{1}{n_0^*}\rho^*, \tag{B.14}$$

$$\nabla^* \cdot \boldsymbol{B}^* = 0, \tag{B.15}$$

where

$$\rho^*(\boldsymbol{x}^*) = \sum_s q_s^* n_s^*(\boldsymbol{x}^*), \tag{B.16}$$

$$\boldsymbol{j}^*(\boldsymbol{x}^*) = \sum_s q_s^* n_s^*(\boldsymbol{x}^*)\boldsymbol{v}_s^*. \tag{B.17}$$

We first advance the velocity $\boldsymbol{v}_{sj}^*$ and the position $\boldsymbol{x}_{sj}^*$ in time, using Equations (B.10) and (B.11). After all particle velocities and positions are determined, we can next obtain the charge density and the current density at each grid point from Equations (B.16) and (B.17), respectively. We finally advance in time the electric field and the magnetic field through Maxwell's equations (B.12) – (B.15). It is noticeable that we separately derive the longitudinal and transversal components of the electric field from (B.14) and (B.13), respectively, to satisfy the charge conservation.

In the following section, we omit the asterisks to avoid the complication.

B.2 Boundary and Initial Conditions

The boundary condition in our simulation is set to be doubly periodic. The initial conditions should be given with self-consistency to the particle position $\boldsymbol{x}_{sj}$ and velocity $\boldsymbol{v}_{sj}$, the fluctuating fields ($\boldsymbol{E}$, $\boldsymbol{B}_1$), and the uniform field $\boldsymbol{B}_0$. The initial distribution of particles are assumed to be Maxwellian obtained by making use of Box-Muller method [*Press et al.*, 1992], by which particle velocities with the thermal velocity v_t are described in the following form,

$$\begin{aligned} v_1 &= v_t\sqrt{-2\ln x_1}\cos 2\pi x_2, \\ v_2 &= v_t\sqrt{-2\ln x_1}\sin 2\pi x_2, \end{aligned} \tag{B.18}$$

where x_1 and x_2 are the uniform random numbers. The velocities v_1 and v_2 are independent of each other.

B.3 Momentum Equations

The finite-difference equations of (B.10) and (B.11) are

$$\frac{\boldsymbol{v}_s^{n+1/2} - \boldsymbol{v}_s^{n-1/2}}{\Delta t} = \frac{q_s}{m_s}\left[\boldsymbol{E}^n(\boldsymbol{x}_s^n) + \frac{\boldsymbol{v}_s^{n+1/2} + \boldsymbol{v}_s^{n-1/2}}{2} \times \boldsymbol{B}^n(\boldsymbol{x}_s^n)\right], \tag{B.19}$$

$$\frac{\boldsymbol{x}_s^{n+1} - \boldsymbol{x}_s^n}{\Delta t} = \boldsymbol{v}_s^{n+1/2}, \tag{B.20}$$

where $(n-1/2,\, n,\, n+1/2)$ represent time grids at $((n-1/2)\Delta t,\, n\Delta t,\, (n+1/2)\Delta t)$. $\boldsymbol{E}(\boldsymbol{x}_s)$ and $\boldsymbol{B}(\boldsymbol{x}_s)$ are the values at the particle position $\boldsymbol{x}_s$. However $\boldsymbol{E}$ and $\boldsymbol{B}$ are defined only at spatial grid points $\boldsymbol{X}_i$. Thus it is necessary to assign the values of electromagnetic field defined at grid points $\boldsymbol{X}_i$ to those at particle positions $\boldsymbol{x}_j$. In our code, we give a particle with a broad shape in the following form,

$$S(x,y) = \frac{(\Delta x - |x|)(\Delta y - |y|)}{\Delta x \Delta y}, \quad |x| \le \Delta x, \quad |y| \le \Delta y, \tag{B.21}$$

where $S(x,y)$ is called the shape factor. Then the assignment to a particle position $\boldsymbol{x}_{sj}$ is conducted from the nearest four grid points (X_i, Y_k), (X_{i+1}, Y_k), (X_i, Y_{k+1}), and (X_{i+1}, Y_{k+1}),

$$\begin{aligned}\boldsymbol{E}(x_j,y_j) = {} & \boldsymbol{E}(X_i,Y_k)S(X_i - x_j, Y_k - y_j) + \boldsymbol{E}(X_i,Y_{k+1})S(X_i - x_j, Y_{k+1} - y_j) \\ & + \boldsymbol{E}(X_{i+1},Y_k)S(X_{i+1} - x_j, Y_k - y_j) + \boldsymbol{E}(X_{i+1},Y_{k+1})S(X_{i+1} - x_j, Y_{k+1} - y_j).\end{aligned}$$

This technique is called the particle-in-cell (PIC) method.

B.4 Charge Assignment

In order to obtain the charge density ρ and the current density j at each grid point $\boldsymbol{X}_i$, it is necessary to assign particle positions $\boldsymbol{x}_{sj}$ and velocities $\boldsymbol{v}_{sj}$ to grid points. In our code, the quantities associated with a particle $(\boldsymbol{x}_{sj},\, \boldsymbol{v}_{sj})$ are assigned to the nearest four grid points by making use of PIC method as is conducted in the previous section. Since the particle velocities are defined at half-integer time, $\rho(\boldsymbol{X}_i)$ and $\boldsymbol{j}(\boldsymbol{X}_i)$ are expressed as

$$\rho^n(\boldsymbol{X}_i) = \sum_s \sum_j q_s S(x_{sj}^n - X_i, y_{sj}^n - Y_k),$$

$$\boldsymbol{j}^{n+1/2}(\boldsymbol{X}_i) = \sum_s \sum_j q_s \boldsymbol{v}_{sj}^{n+1/2} \frac{S(x_{sj}^n - X_i, y_{sj}^n - Y_k) + S(x_{sj}^{n+1} - X_i, y_{sj}^{n+1} - Y_k)}{2}.$$

B.5 Poisson's Equation

After the spatial distribution of the charge density are derived, we can obtain the longitudinal electric field $\boldsymbol{E}_L$ from Poisson's equation,

$$\nabla \cdot \boldsymbol{E}_L|_{\boldsymbol{X}_i} = \frac{1}{n_0}\rho(\boldsymbol{X}_i). \tag{B.22}$$

We solve Equation (B.22) by executing Fourier transformation. Since $\boldsymbol{E}_L$ can be expressed by a scalar potential ϕ in the form,

$$\boldsymbol{E}_L(\boldsymbol{X}_i) = -\nabla\phi|_{\boldsymbol{X}_i}. \tag{B.23}$$

(B.22) is rewritten as

$$\nabla^2\phi|_{\boldsymbol{X}_i} = -\frac{1}{n_0}\rho(\boldsymbol{X}_i). \tag{B.24}$$

Here we write the position of grid points with the integer l and m,

$$\begin{aligned}
&\boldsymbol{X}_i = l\,\Delta x\hat{\boldsymbol{e}}_x + m\,\Delta y\hat{\boldsymbol{e}}_y,\\
&\qquad l = 0, 1, \cdots, N_x - 1 \qquad N_x : \text{the number of grids in the } x \text{ direction},\\
&\qquad m = 0, 1, \cdots, N_y - 1 \qquad N_y : \text{the number of grids in the } y \text{ direction},
\end{aligned}$$

and the physical quantities at the grid points as $A_{l,m}$.

The Fourier transformation in the discrete form is, for example,

$$\rho_{k_x,k_y} = \Delta x\Delta y \sum_l \sum_m \rho_{l,m} e^{-i(k_x x_l + k_y y_m)}, \tag{B.25}$$

where

$$\begin{aligned}
&(x_l, y_m) = (l\Delta_x, m\Delta_y),\\
&(k_x, k_y) = \left(\frac{2\pi n_x}{N_x\Delta_x}, \frac{2\pi n_y}{N_y\Delta_y}\right),\\
&\qquad n_{x,y} = 0, \pm 1, \pm 2, \cdots, \pm\frac{N_{x,y}}{2} - 1, -\frac{N_{x,y}}{2}.
\end{aligned} \tag{B.26}$$

On the other hand, the inverse Fourier transformation in the discrete form is

$$\rho_{l,m} = \frac{1}{(N_x\Delta x)(N_y\Delta y)} \sum_{n_x=-N_x/2}^{N_x/2-1} \sum_{n_y=-N_y/2}^{N_y/2-1} \rho_{k_x,k_y} e^{i(k_x x_l + k_y y_m)}. \tag{B.27}$$

The finite-difference equation of (B.24) is

$$\frac{\phi_{l+1,m} - 2\phi_{l,m} + \phi_{l-1,m}}{\Delta x^2} + \frac{\phi_{l,m+1} - 2\phi_{l,m} + \phi_{l,m-1}}{\Delta y^2} = -\frac{n_0}{\rho_{l,m}}.$$

And its Fourier transformation is

$$K_{\boldsymbol{k}}^2 \phi_{\boldsymbol{k}} = \frac{\rho_{\boldsymbol{k}}}{n_0}, \tag{B.28}$$

where

$$K_{\boldsymbol{k}}^2 = k_x^2 \mathrm{dif}^{\,2}\left(\frac{k_x \Delta x}{2}\right) + k_y^2 \mathrm{dif}^{\,2}\left(\frac{k_y \Delta y}{2}\right), \qquad \mathrm{dif}\,\theta \equiv \frac{\sin\theta}{\theta}.$$

Then the finite-difference form of the x component of Equation (B.23) is

$$E_{x,l,m} = -\frac{\phi_{l+1,m} - \phi_{i-1,m}}{2\Delta x}.$$

And its Fourer transformation is

$$E_{x,\boldsymbol{k}} = -i\kappa_{x,\boldsymbol{k}} \phi_{\boldsymbol{k}}, \qquad \text{where} \quad \kappa_{x,\boldsymbol{k}} = k_x \mathrm{dif}\,(k_x \Delta x). \tag{B.29}$$

From (B.28) and (B.29), we can obtain

$$E_{x,\boldsymbol{k}} = -i\frac{\kappa_{x,\boldsymbol{k}}}{n_0 K_{\boldsymbol{k}}^2}\,\rho_{\boldsymbol{k}}. \tag{B.30}$$

In the same way, we can get the y component,

$$E_{y,\boldsymbol{k}} = -i\frac{\kappa_{y,\boldsymbol{k}}}{n_0 K_{\boldsymbol{k}}^2}\,\rho_{\boldsymbol{k}}. \tag{B.31}$$

The longitudinal electric field $\boldsymbol{E}_L$ is derived by the inverse Fourier transforming of (B.30) and (B.31).

B.6 Faraday's Law and Ampère's Law

We finally advance the fluctuating magnetic field and the transversal electric field, using Faraday's law and Ampère's law. The finite-difference form of Equations (B.12) and (B.13) is

$$\frac{\boldsymbol{B}^{n+1} - \boldsymbol{B}^n}{\Delta t} = -\nabla \times \left(\frac{\boldsymbol{E}_T^{n+1} + \boldsymbol{E}_T^n}{2}\right), \tag{B.32}$$

$$\frac{\boldsymbol{E}_T^{n+1} - \boldsymbol{E}_T^n}{\Delta t} = \nabla \times \left(\frac{\boldsymbol{B}^{n+1} + \boldsymbol{B}^n}{2}\right) - \frac{1}{n_0}\boldsymbol{j}_T^{n+1/2}, \tag{B.33}$$

where the suffix T denotes the transversal component of the quantity. Combining (B.32) and (B.33), we eliminate $\boldsymbol{B}^{n+1}$ to obtain $\boldsymbol{E}_T^{n+1}$ from the previously given quantities ($\boldsymbol{E}_T^n$, $\boldsymbol{B}^n$, $\boldsymbol{j}_T^{n+1/2}$),

$$\left[1+\frac{\Delta t^2}{4}\nabla\times\nabla\times\right]\boldsymbol{E}_T^{n+1}=\left[1-\frac{\Delta t^2}{4}\nabla\times\nabla\times\right]\boldsymbol{E}_T^{n}+\Delta t\nabla\times\boldsymbol{B}^n-\frac{\Delta t}{n_0}\boldsymbol{j}_T^{n+1/2}. \quad \text{(B.34)}$$

Here, making use of the notation $\nabla\times\nabla\times\boldsymbol{E}_T=-\nabla^2\boldsymbol{E}_T$, we rewrite the above equation as

$$\left[1-\frac{\Delta t^2}{4}\nabla^2\right]\boldsymbol{E}_T^{n+1}=\left[1+\frac{\Delta t^2}{4}\nabla^2\right]\boldsymbol{E}_T^{n}+\Delta t\nabla\times\boldsymbol{B}^n-\frac{\Delta t}{n_0}\boldsymbol{j}_T^{n+1/2}. \quad \text{(B.35)}$$

In Equation (B.35), the finite-difference forms of the terms including ∇ operator are

$$\nabla^2\boldsymbol{E}=\frac{\boldsymbol{E}_{l+1,m}-2\boldsymbol{E}_{l,m}+\boldsymbol{E}_{l-1,m}}{\Delta x^2}+\frac{\boldsymbol{E}_{l,m+1}-2\boldsymbol{E}_{l,m}+\boldsymbol{E}_{l,m-1}}{\Delta y^2},$$

$$\nabla\times\boldsymbol{B}=\begin{bmatrix}\frac{B_{z,l,m+1}-B_{z,l,m-1}}{2\Delta y}\\ -\frac{B_{z,l+1,m}-B_{z,l-1,m}}{2\Delta x}\\ \frac{B_{y,l+1,m}-B_{y,l-1,m}}{2\Delta x}-\frac{B_{x,l,m+1}-B_{x,l,m-1}}{2\Delta y}\end{bmatrix}.$$

Thus the Fourier transformation of (B.35) is

$$\left[1+\frac{\Delta t^2}{4}K_{\boldsymbol{k}}^2\right]\boldsymbol{E}_{\boldsymbol{k}}^{n+1}=\left[1-\frac{\Delta t^2}{4}K_{\boldsymbol{k}}^2\right]\boldsymbol{E}_{\boldsymbol{k}}^{n}+i\Delta t\,\boldsymbol{\kappa}_{\boldsymbol{k}}\times\boldsymbol{B}_{\boldsymbol{k}}^n-\frac{\Delta t}{n_0}\boldsymbol{j}_{\boldsymbol{k}}^{n+1/2}, \quad \text{(B.36)}$$

where $(\boldsymbol{E}_{\boldsymbol{k}}^{n+1},\boldsymbol{E}_{\boldsymbol{k}}^{n},\boldsymbol{B}_{\boldsymbol{k}}^{n},\boldsymbol{j}_{\boldsymbol{k}}^{n+1/2})$ are the Fourier components of $(\boldsymbol{E}_T^{n+1},\boldsymbol{E}_T^{n},\boldsymbol{B}^{n},\boldsymbol{j}_T^{n+1/2})$, respectively, and $K_{\boldsymbol{k}}^2$ and $\boldsymbol{\kappa}_{\boldsymbol{k}}$ are defined as the following forms,

$$K_{\boldsymbol{k}}^2=k_x^2\mathrm{dif}^2\left(\frac{k_x\Delta x}{2}\right)+k_y^2\mathrm{dif}^2\left(\frac{k_y\Delta y}{2}\right),$$

$$\boldsymbol{\kappa}_{\boldsymbol{k}}=\begin{bmatrix}k_x\mathrm{dif}\,(k_x\Delta x)\\ k_y\mathrm{dif}\,(k_y\Delta y)\\ 0\end{bmatrix}.$$

Then we can calculate $\boldsymbol{B}_{\boldsymbol{k}}^{n+1}$, the Fourier component of $\boldsymbol{B}^{n+1}$, by Fourier transforming Equation (B.32).

$$\boldsymbol{B}_{\boldsymbol{k}}^{n+1}=\boldsymbol{B}_{\boldsymbol{k}}^{n}-i\Delta t\,\boldsymbol{\kappa}_{\boldsymbol{k}}\times\left(\frac{\boldsymbol{E}_{\boldsymbol{k}}^{n+1}+\boldsymbol{E}_{\boldsymbol{k}}^{n}}{2}\right). \quad \text{(B.37)}$$

The advanced electromagnetic fields ($\boldsymbol{E}_T^{n+1}$, $\boldsymbol{B}^{n+1}$) are obtained by inversely Fourier transforming ($\boldsymbol{E}_{\boldsymbol{k}}^{n+1}$, $\boldsymbol{B}_{\boldsymbol{k}}^{n+1}$).

References

Baumjohann, W., G. Paschmann, and C. A. Cattell, Average plasma properties in the central plasma sheet, *J. Geophys. Res.*, **94**, 6597-6606, 1989.

Baumjohann, W., G. Paschmann, T. Nagai, and H. Lühr, Superposed epoch analysis of the substorm plasma sheet, *J. Geophys. Res.*, **96**, 11,605-11,608, 1991.

Birdsall, C. K., and A. B. Langdon, *Plasma physics via computer simulation*, Institute of Physics, London, 1995.

Coroniti, F. V., and A. Eviatar, Magnetic field reconnection in a collisionless plasma, *Astrophys. J. Suppl. Ser.*, **33**, 189-210, 1977.

Davidson, R. C., N. T. Gladd, C. S. Wu, and J. D. Huba, Effects of finite plasma beta on the lower-hybrid-drift instability, *Phys. Fluids*, **20**, 301-310, 1977.

Forslund, D. W., R. L. Morse, and C. W. Nielson, Electron cyclotron drift instability, *Phys. Rev. Lett.*, **25**, 1266-1270, 1970.

Forslund, D., R. Morse, and C. Nielson, and J. Wu, Electron cyclotron drift instability and turbulence, *Phys. Fluids*, **15**, 1303-1318, 1972.

Fried, B. D. and S. D. Conte, *The plasma dispersion function*, Academic Press, New York and London, 1961.

Gary S. P. and J. J. Sanderson, Longitudinal waves in a perpendicular collisionless plasma shock I. Cold ions, *J. Plasma Phys.*, **4**, 739-751, 1970.

Gary S. P., Longitudinal waves in a perpendicular collisionless plasma shock II. Vlasov ions, *J. Plasma Phys.*, **4**, 753-760, 1970.

Hesse, M. and D. Winske, Hybrid simulations of collisionless reconnection in current sheets, *J. Geophys. Res.*, **99**, 11,177-11,192, 1994.

Hesse, M. and D. Winske, Electron dissipation in collisionless magnetic reconnection, *J. Geophys. Res.*, **103**, 26,479-26,486, 1998.

Hesse, M., K. Schindler, J. Birn, and M. Kuznetsova, The diffusion region in collisionless magnetic reconnection, *Phys. Plasmas*, **6**, 1781-1795, 1999.

Hoshino, M., T. Mukai, T. Yamamoto, and S. Kokubun, Ion dynamics in magnetic reconnection: Comparison between numerical simulation and Geotail observations, *J. Geophys. Res.*, **103**, 4509-4530, 1998.

Hoshino, M., K. Hiraide, and T. Mukai, Strong electron heating and non-Maxwellian behavior in magnetic reconnection, *Earth Planets Space*, **53**, 627-634, 2001a.

Hoshino, M., T. Mukai, T. Terasawa, and I. Shinohara, Suprathermal electron acceleration in magnetic reconnection, *J. Geophys. Res.*, **106**, 25,979-25,997, 2001b.

Huba, J. D., N. T. Gladd, and K. Papadopoulos, Lower-hybrid-drift wave turbulence in the distant magnetotail, *J. Geophys. Res.*, **83**, 5217-5226, 1978.

Kall, N. A. and P. C. Liewer, Low frequency instabilities in magnetic pulses, *Phys. Rev. A*, **4**, 2094-2103, 1971.

Lemons, D. S. and S. P. Gary, Electromagnetic effects on the modified two-stream instability, *J. Geophys. Res.*, **82**, 2337-2342, 1977.

Lin, Y. and D. W. Swift, A two-dimensional hybrid simulation of the magnetotail reconnection layer, *J. Geophys. Res.*, **101**, 19,859-19,870, 1996.

Mandt, M. E., R. E. Denton, and J. F. Drake, Transition to whistler mediated magnetic reconnection, *Geophys. Res. Lett.*, **21**, 73-76, 1994.

McBride, J. B., E. Ott, J. P. Boris, and J. H. Orens, Theory and simulation of turbulent heating by the modified two-stream instability, *Phys. Fluids*, **15**, 2367-2383, 1972.

Nagai, T., M. Fujimoto, Y. Sato, S. Machida, T. Terasawa, R. Nakamura, T. Yamamoto, T. Mukai, A. Nishida, and S. Kokubun, Structure and dynamics of magnetic reconnection for substorm onsets with Geotail observations, *J. Geophys. Res.*, **103**, 4419-4440, 1998.

Nagai, T., I. Shinohara, M. Fujimoto, M. Hoshino, Y. Saito, S. Machida, and T. Mukai, Geotail observations of the Hall current system: Evidence of magnetic reconnection in the magnetotail, *J. Geophys. Res.*, **106**, 25,929-25,949, 2001.

Nakabayashi, J. and S. Machida, Electromagnetic hybrid-code simulation of magnetic reconnection: Velocity distribution functions of accelarated ions, *Geophys. Res. Lett.*, **24**, 1339-1342, 1997.

Nakamura, M. S., M. Fujimoto, and K. Maezawa, Ion dynamics and resaltant velocity space distribution functions in the cource of magnetic reconnection, *J. Geophys. Res.*, **103**, 4531-4546, 1998.

Nicholson, D. R., *Introduction to plasma theory*, John Wiley & Sons, New York, 1983.

Parker, E. N., The solar-flare phenomenon and the theory of reconnection and annihilation of magnetic fields, *Astrophys. J., Suppl. Ser.*, **8**, 177-212, 1963.

Press, W. H., S. A. Teukolsky, W. T. Vetterling, and B. P. Flannery, *Numerical recipes in FORTRAN, 2nd ed.*, Cambridge University Press, New York, 1992.

Sergeev, V. A., V. Angelopoulos, D. G. Mitchell, and C. T. Russell, In situ observations of magnetotail reconnection prior to the onset of a small substorm, *J. Geophys. Res.*, **101**, 19,121-19,133, 1995.

Shay, M. A., J. F. Drake, R. E. Denton, and D. Biskamp, Structure of the dissipation region during collisionless magnetic reconnection, *J. Geophys. Res.*, **103**, 9165-9176, 1998.

Shay, M. A., J. F. Drake, and B. N. Rogers, Alfvénic collisionless magnetic reconnection and the Hall term, *J. Geophys. Res.*, 106, 3759-3772, 2001.

Shinohara, I., T. Nagai, M. Fujimoto, T. Terasawa, T. Mukai, K. Tsuruda, and T. Yamamoto, Low-frequency electromagnetic turburence observed near the substorm onset site, *J. Geophy. Res.*, **103**, 20,365-20,388, 1998.

Sonnerup, B. U. Ö., Magnetic field reconnection, in *Solar System Plasma Physics*, vol. III, edited by L. J. Lanzerotti, C. F. Kennel, and E. N. Parker, pp. 45-108, North-Holland, Amsterdam, 1979.

Sweet, P. A., The neutral point theory of solar flares, in *Electromagnetic Phenomena in Cosmical Physics*, edited by B. Lehnert, pp. 123-134, Cambridge University Press, London, 1958.

Tanaka, M., Macro-particle simulations of collisionless magnetic reconnection, *Phys. Plasmas*, **2**, 2920-2930, 1995.

Tsai, S. T., M. Tanaka, J. D. Gaffey, Jr., E. H. Da Jornada, C. S. Wu, and L. F. Ziebell, Effect of electron thermal anisotropy on the kinetic cross-field streaming instability, *J. Plasma Phys.*, **32**, 159-178, 1984.

Winske, D., M. Tanaka, C. S. Wu, and K. B. Quest, Plasmaheating at collisionless shocks due to the kinetic cross-field streaming instability, *J. Geophys. Res.*, **90**, 123-136, 1985.

Wong, H. V., Electrostatic electron-ion streaming instability, *Phys. Fluids*, **13**, 757-760, 1970.

Wu, C. S., Y. M. Zhou, S. C. Guo, D. Winske, and K. Papadopoulos, A kinetic cross-field streaming instability, *Phys. Fluids*, **26**, 1259-1267, 1983.

List of Figures

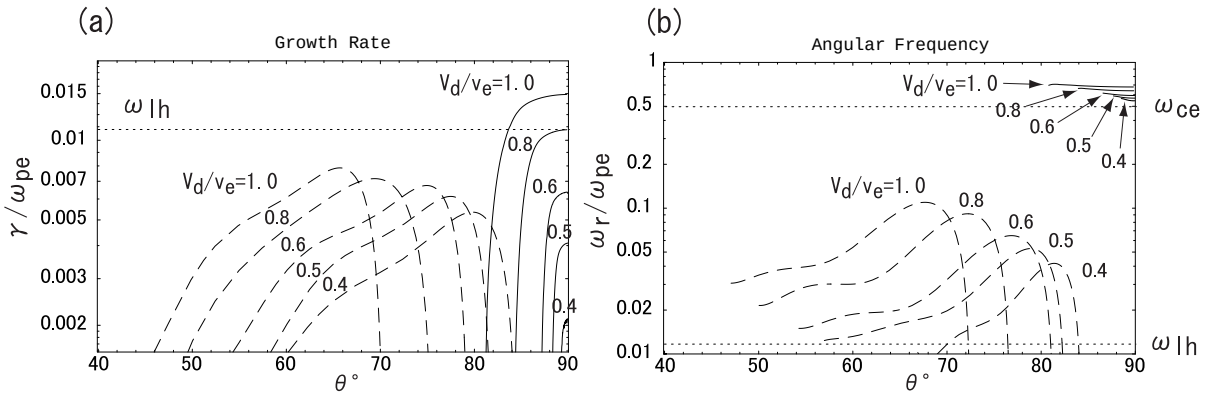

Figure 1.

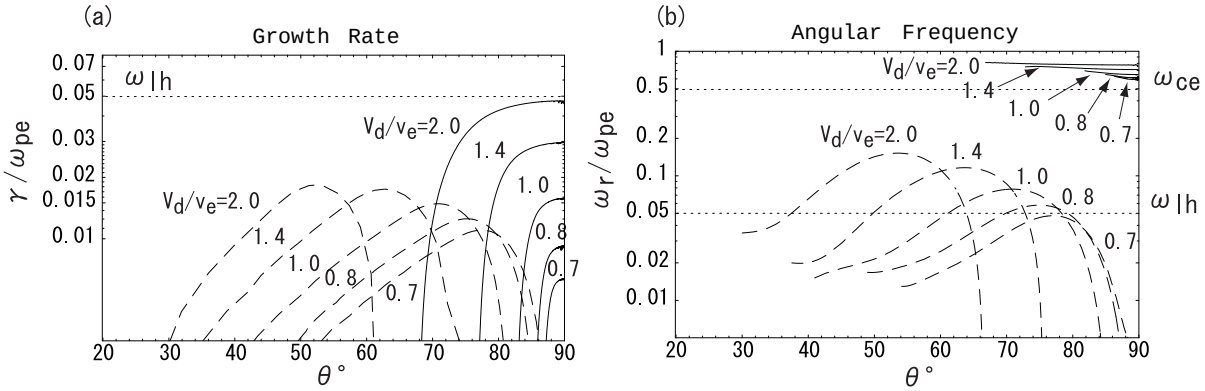

Figure 2.

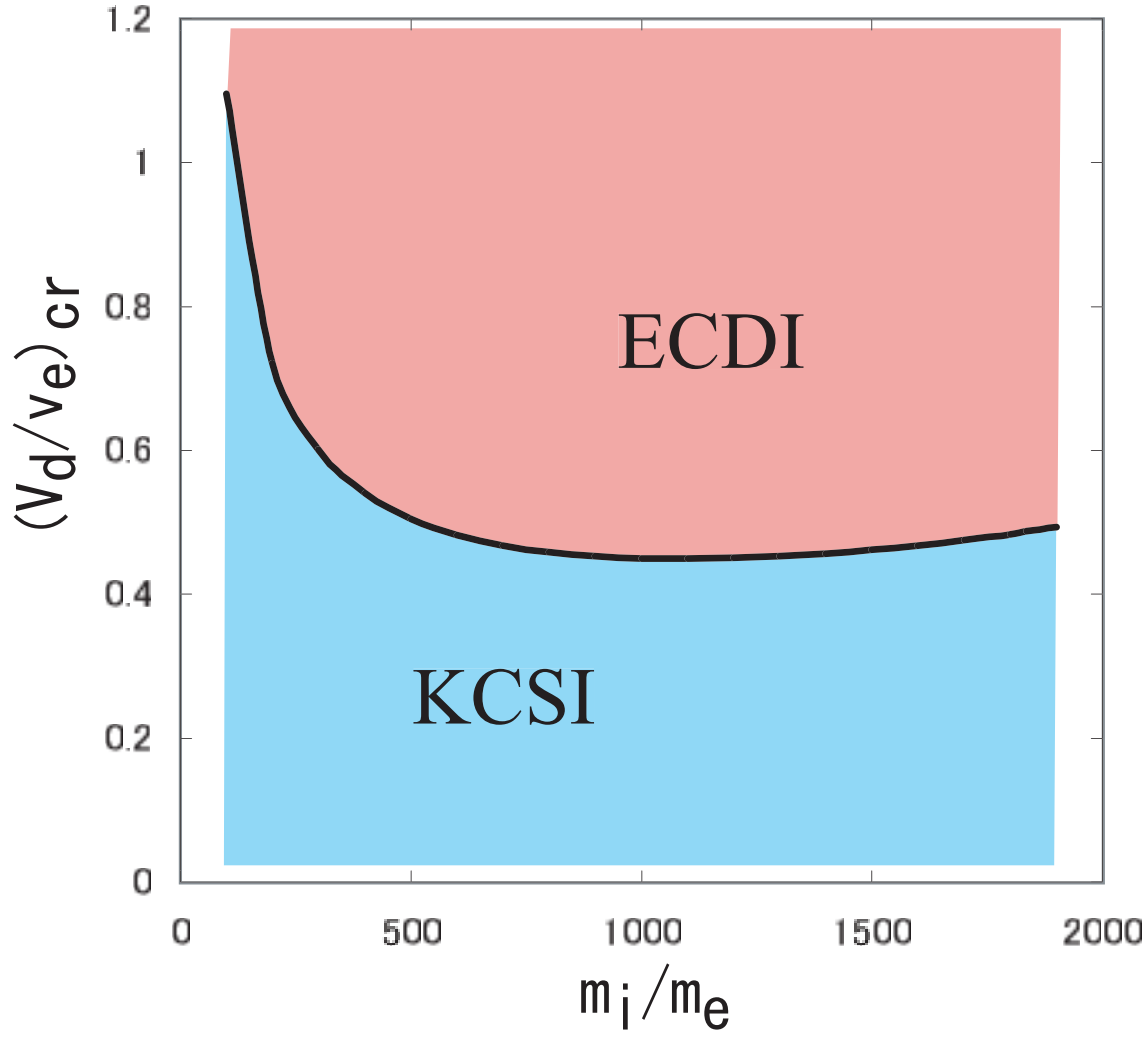

Figure 3.

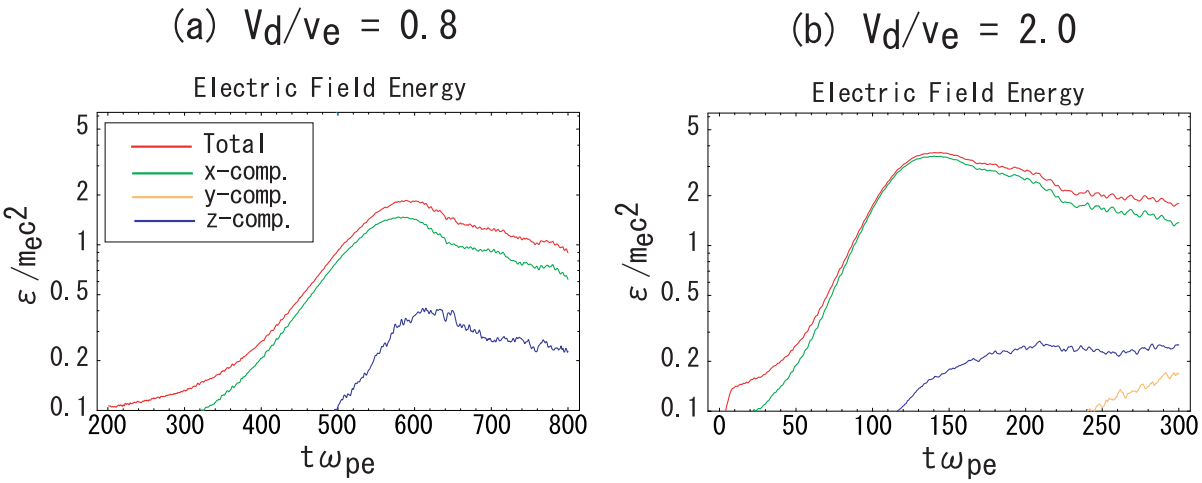
(a) Vd/ve = 0.8
Electric Field Energy
Total
x-comp.
y-comp.
z-comp.
ε /mec2
tωpe
(b) Vd/ve = 2.0
Electric Field Energy
ε /mec2
tωpe

Figure 4.

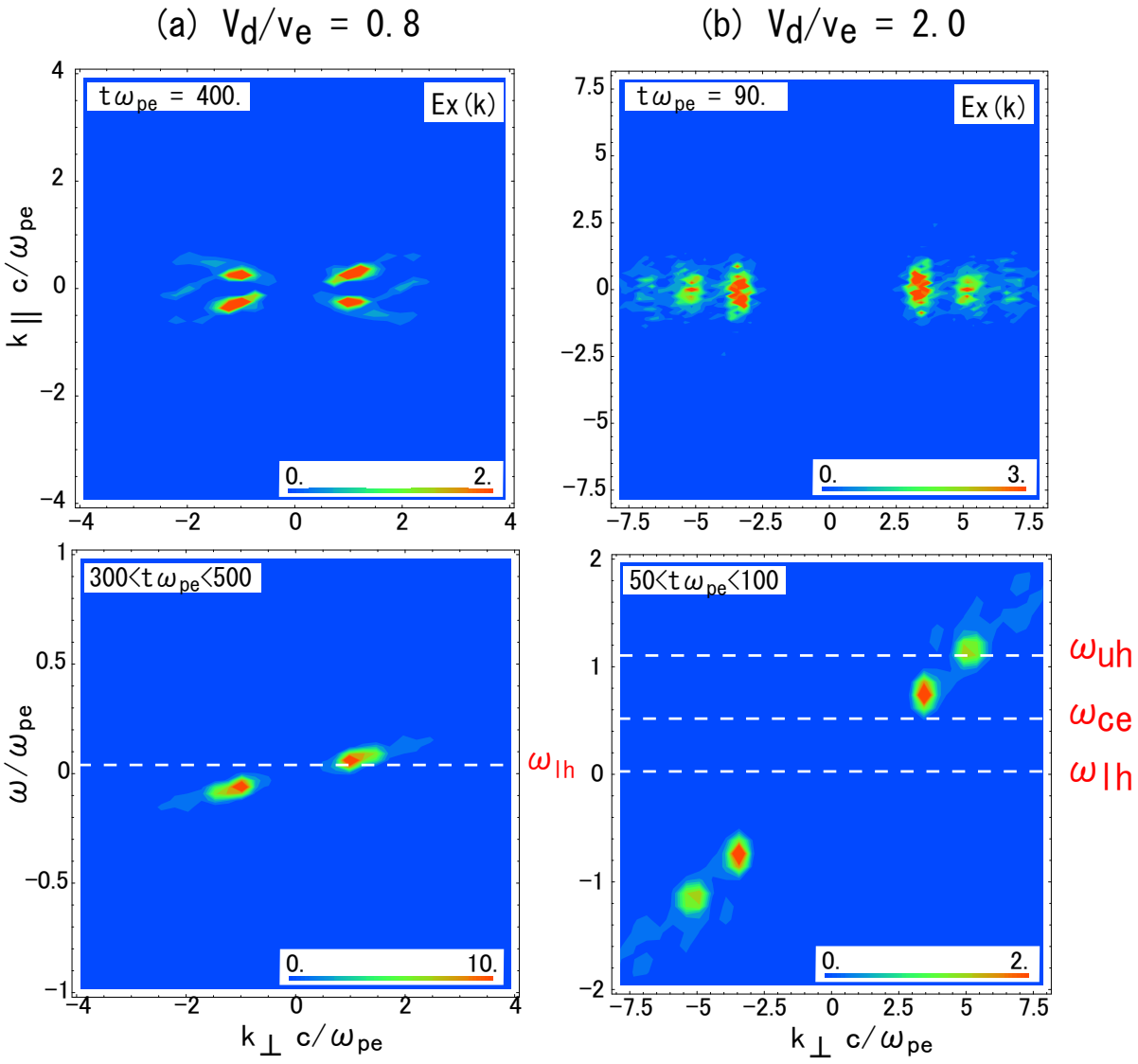
(a) Vd/ve = 0.8
(b) Vd/ve = 2.0
tωpe = 400.
Ex (k)
0. 2.
tωpe = 90.
Ex (k)
0. 3.
k || c/ωpe
300<tωpe<500
0. 10.
ω/ωpe
ωlh
50<tωpe<100
0. 2.
ωuh
ωce
ωlh
k⊥ c/ωpe
k⊥ c/ωpe

Figure 5.

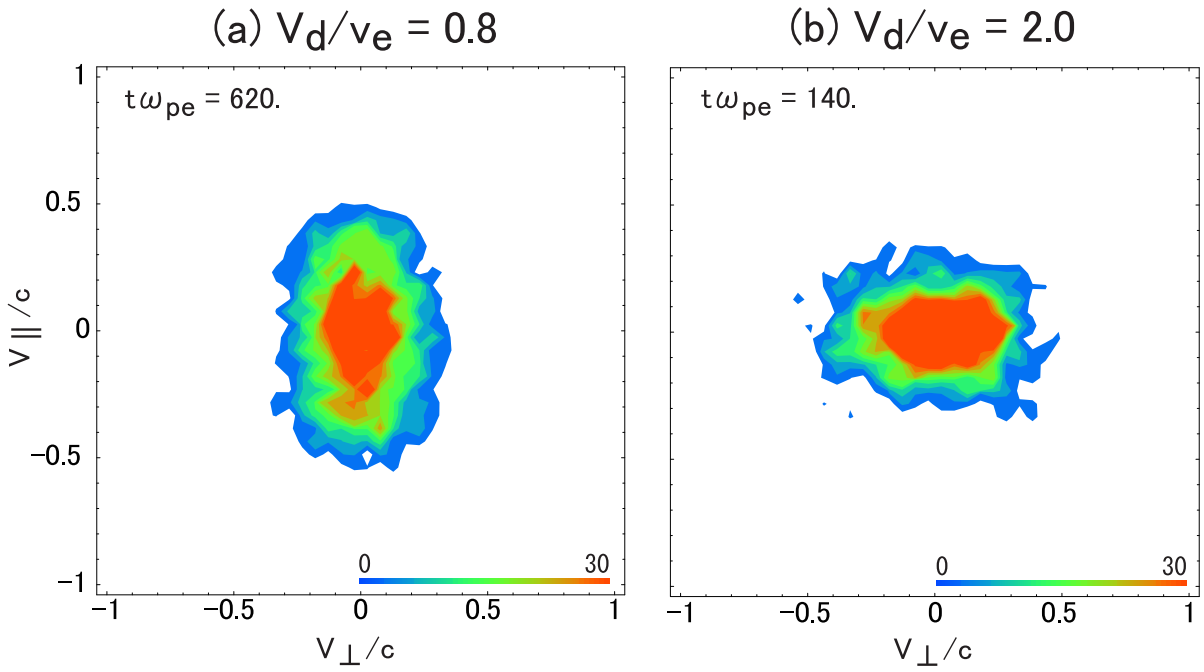

Figure 6.

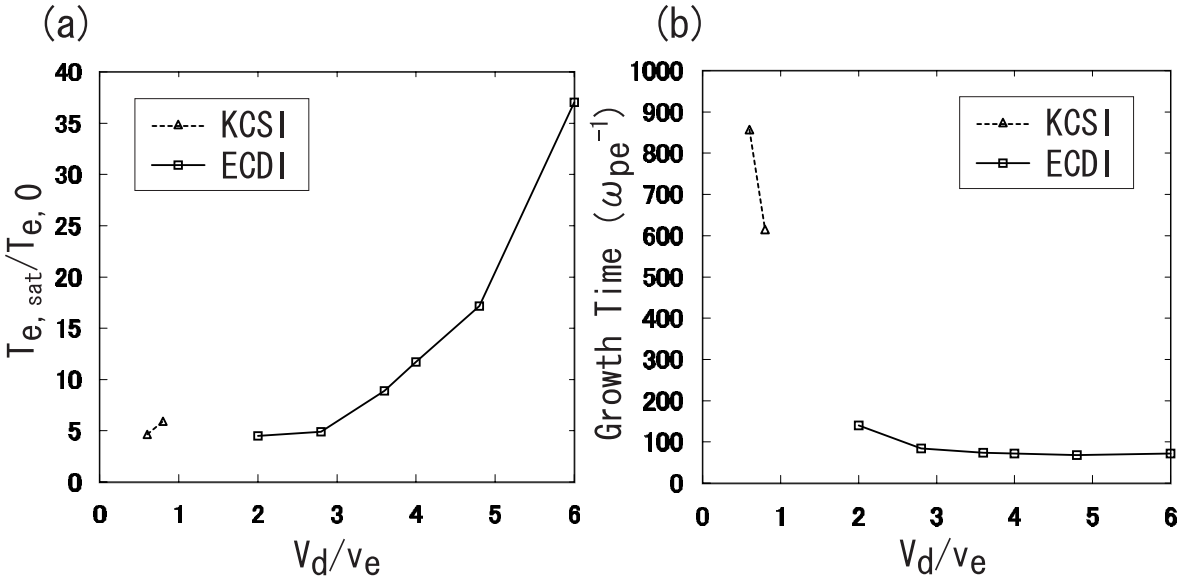

Figure 7.

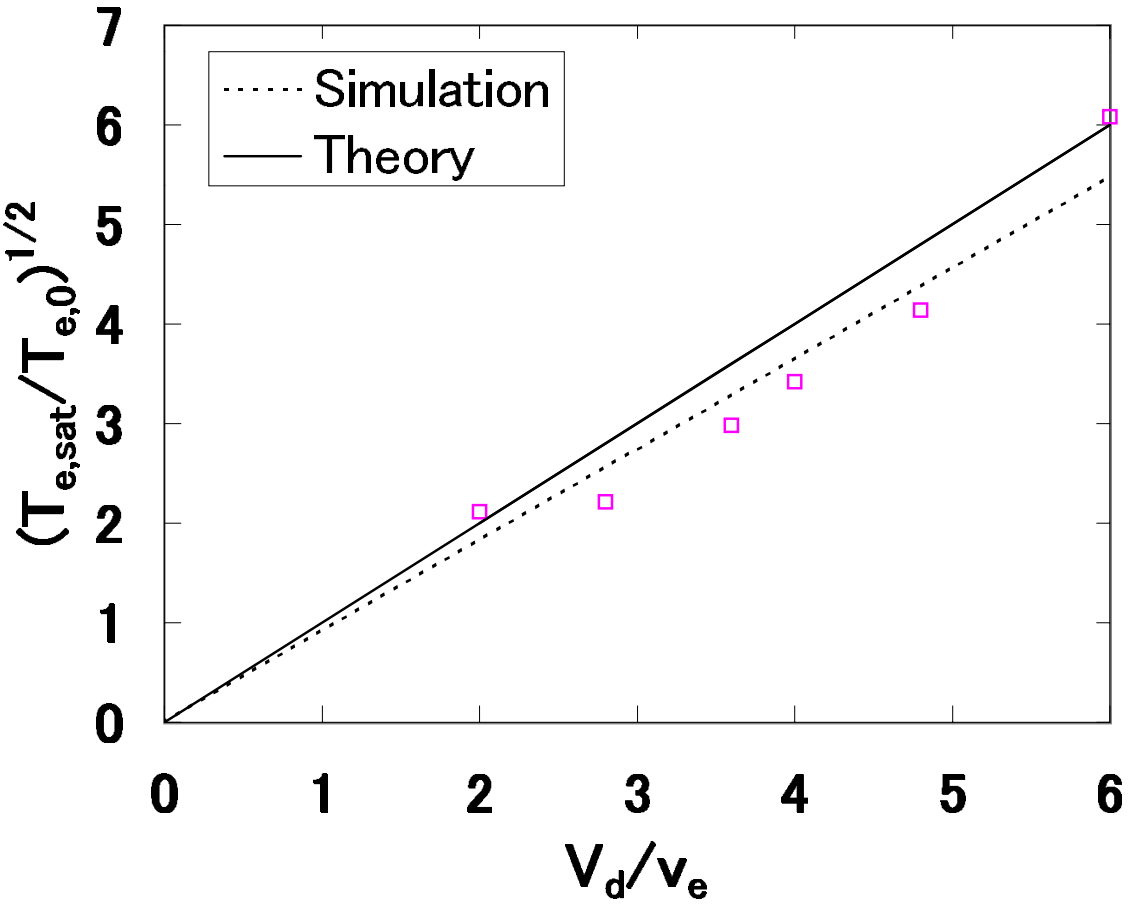

Figure 8.

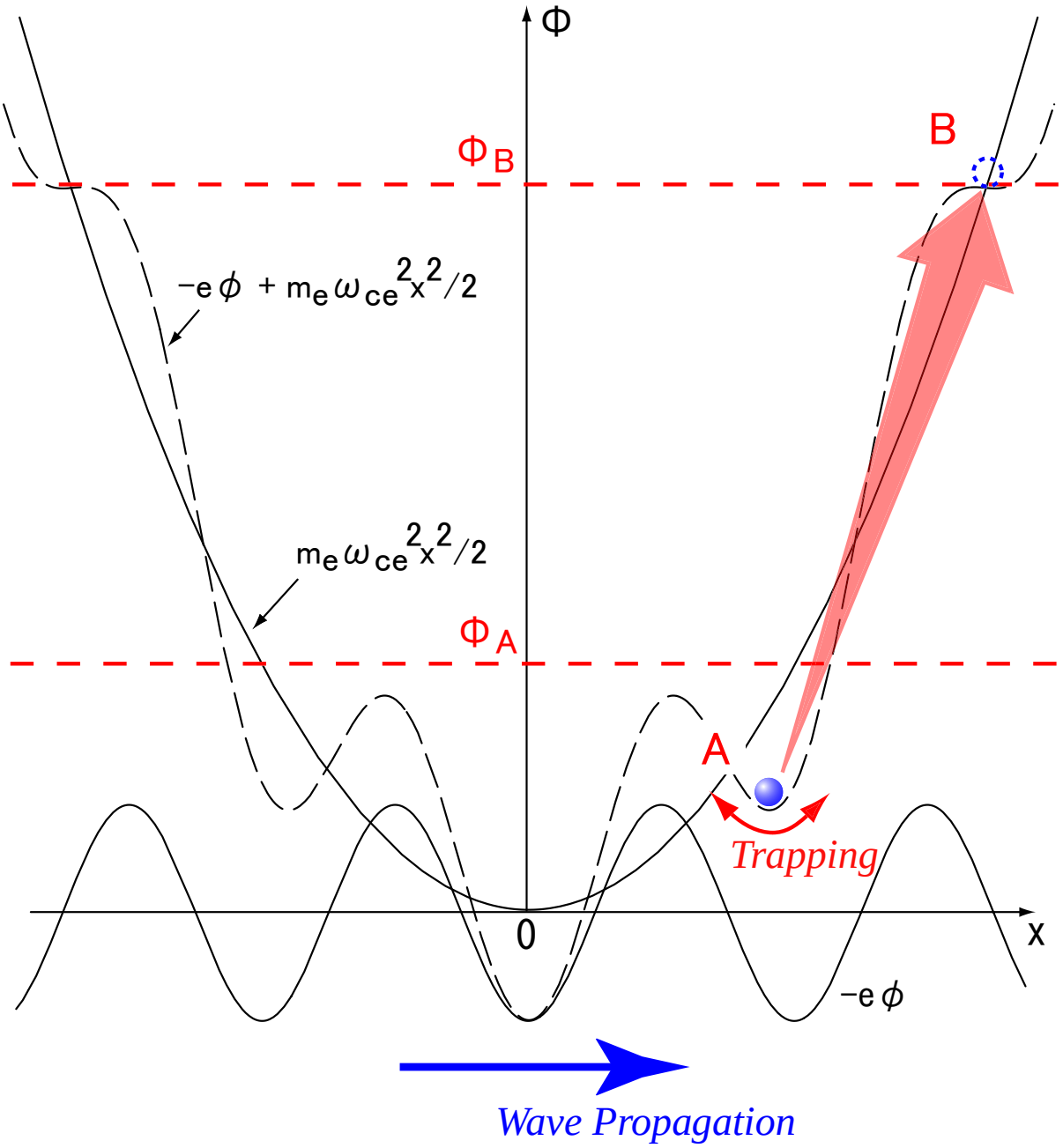
Φ
Φ B
B
−e ϕ + m e ω ce 2 x 2 /2
m e ω ce 2 x 2 /2
Φ A
A
Trapping
0
x
−e ϕ
Wave Propagation

Figure 9.

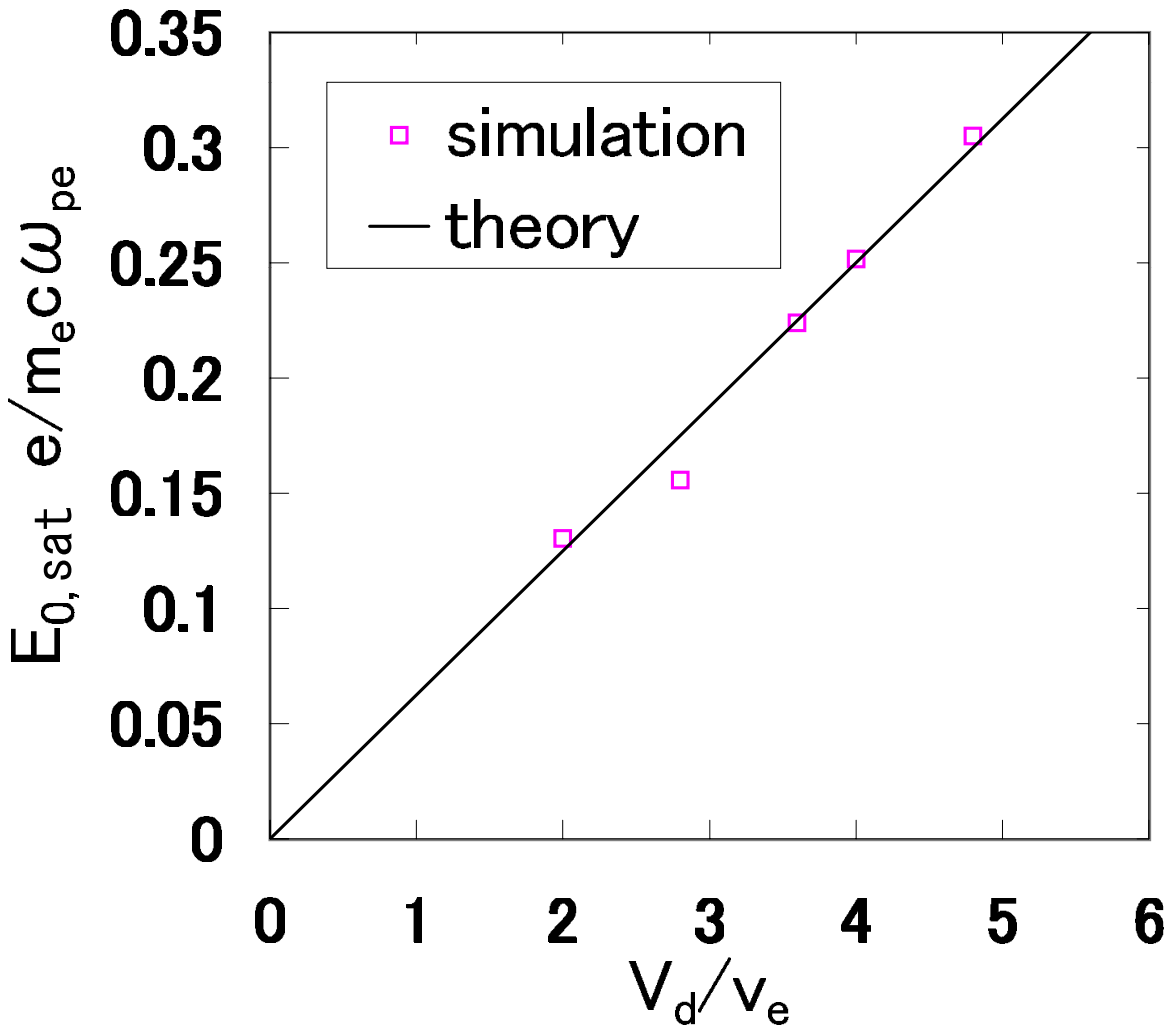
0.35
0.3
0.25
0.2
0.15
0.1
0.05
0
0
1
2
3
4
5
6
simulation
theory
$E_{0,sat}\ e/m_e c\omega_{pe}$
V_d/v_e

Figure 10.

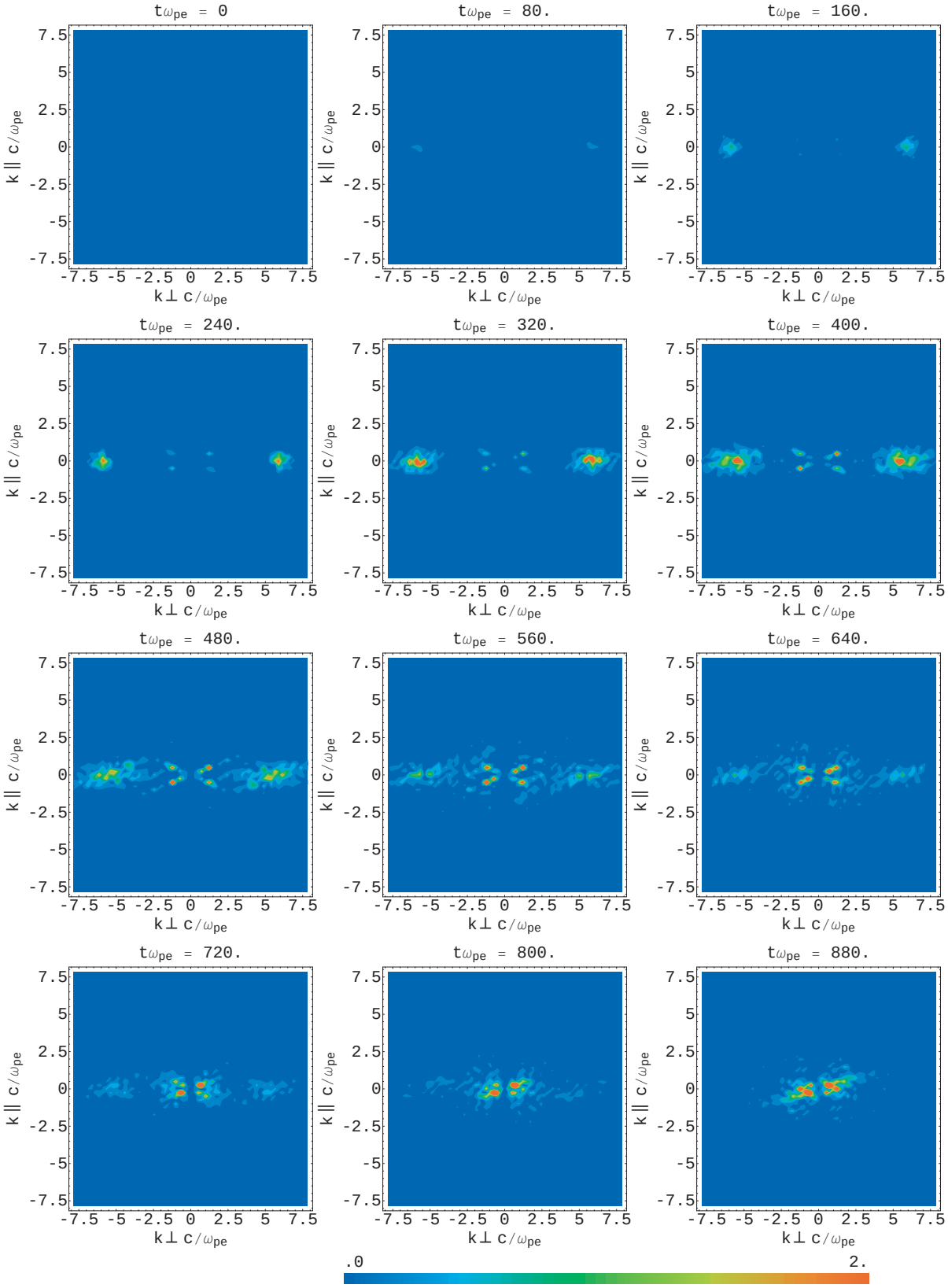
tωpe = 0
tωpe = 80.
tωpe = 160.
tωpe = 240.
tωpe = 320.
tωpe = 400.
tωpe = 480.
tωpe = 560.
tωpe = 640.
tωpe = 720.
tωpe = 800.
tωpe = 880.
k∥ c/ωpe
k⊥ c/ωpe
7.5
5
2.5
0
-2.5
-5
-7.5
.0
2.

Figure 11.

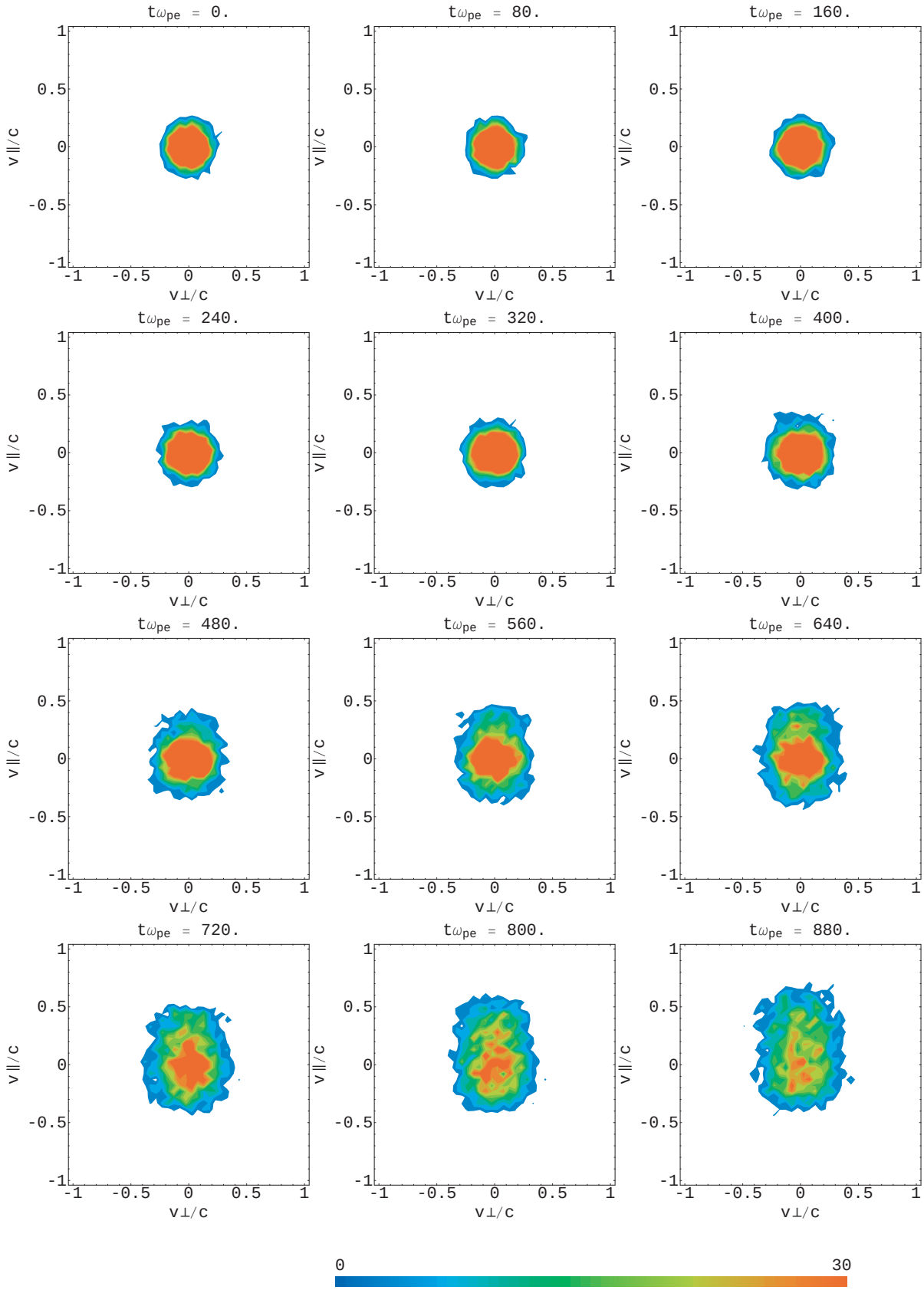
tωpe = 0.
tωpe = 80.
tωpe = 160.
tωpe = 240.
tωpe = 320.
tωpe = 400.
tωpe = 480.
tωpe = 560.
tωpe = 640.
tωpe = 720.
tωpe = 800.
tωpe = 880.
v∥/c
v⊥/c
1
0.5
0
-0.5
-1
0
30

Figure 12.

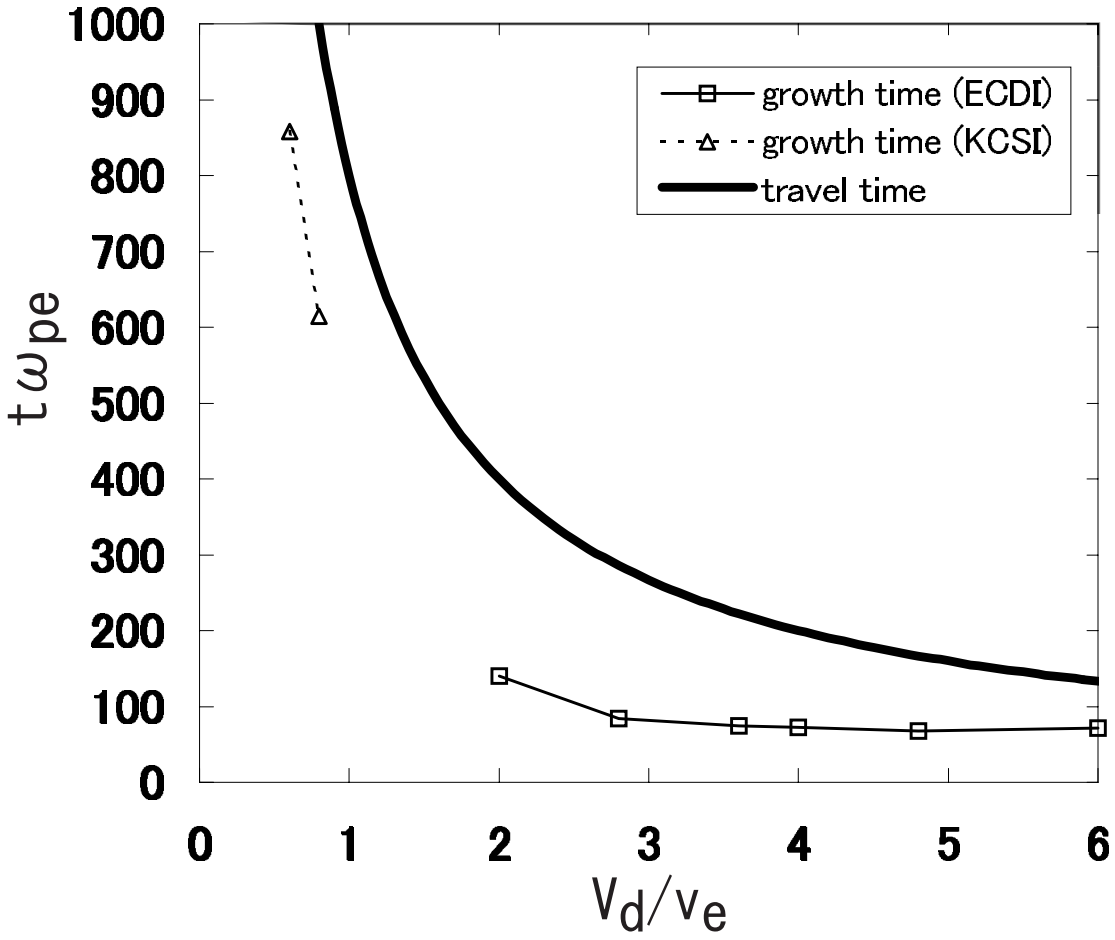
1000
900
800
700
600
500
400
300
200
100
0
tωpe
0
1
2
3
4
5
6
Vd/ve
growth time (ECDI)
growth time (KCSI)
travel time

Figure 13.

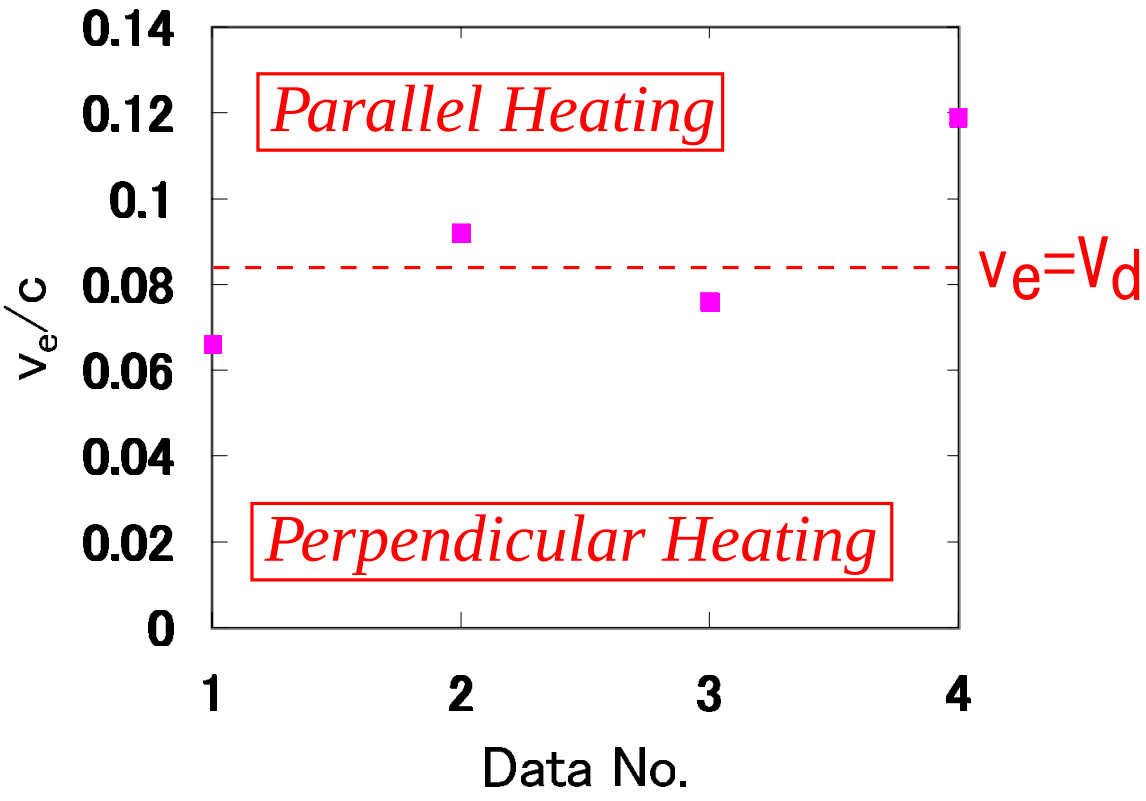
0.14
0.12
0.1
0.08
0.06
0.04
0.02
0
v_e/c
Parallel Heating
Perpendicular Heating
$v_e=V_d$
1
2
3
4
Data No.

Figure 14.

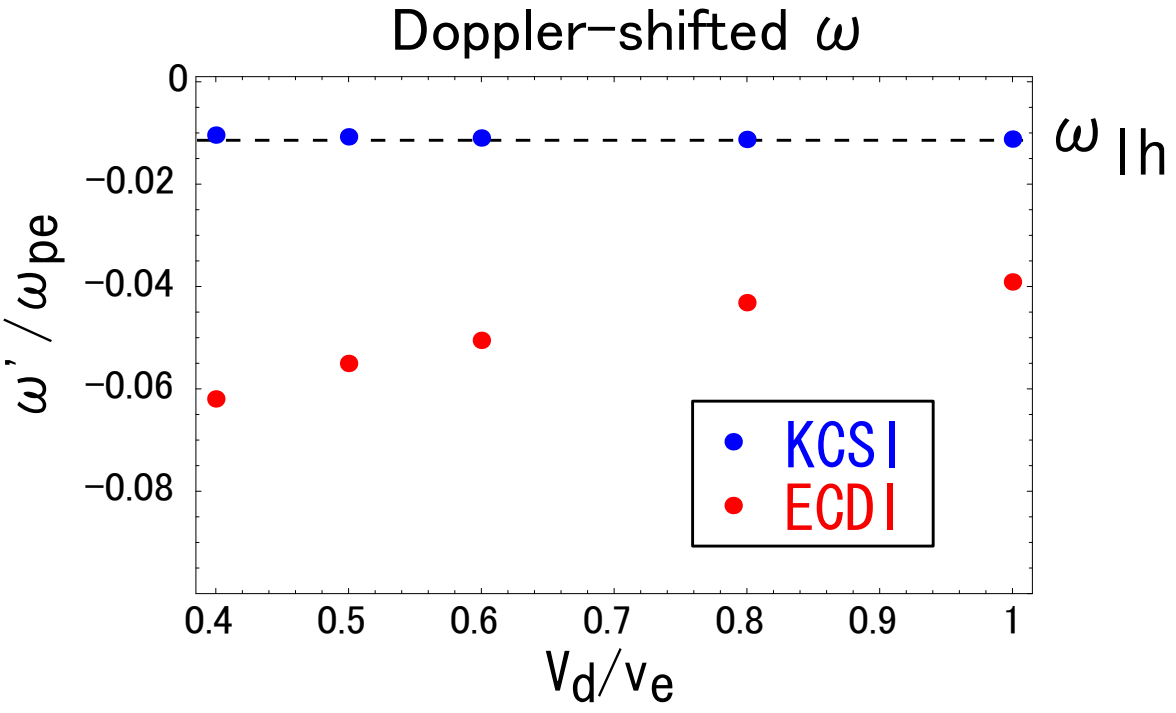
Doppler−shifted ω
0
−0.02
−0.04
−0.06
−0.08
ω'/ωpe
ω lh
KCSI
ECDI
0.4
0.5
0.6
0.7
0.8
0.9
1
Vd/ve

Figure 15.